J. Fluid Mech. (1995), *vol.* 291, *pp.* 191–222

Quasi-periodic cylinder wakes and the Ginzburg–Landau model

By PIERRE ALBARÈDE† AND MICHEL PROVANSAL

Laboratoire de Recherche en Combustion, Université de Provence-CNRS, 13397 Marseille CEDEX 13, France

(Received 16 July 1993 and in revised form 19 December 1994)

The time-periodic phenomena occurring at low Reynolds numbers ($Re \lesssim 180$) in the wake of a circular cylinder (finite-length section) are well modelled by a Ginzburg–Landau (GL) equation with zero boundary conditions (Albarède & Monkewitz 1992). According to the GL model, the wake is mainly governed by a rescaled length, based on the aspect ratio and the Reynolds number. However, the determination of coefficients is not complete: we correct a former evaluation of the nonlinear Landau coefficient, we show difficulties in obtaining a consistent set of coefficients for different Reynolds numbers or end configurations, and we propose the use of an 'influential' length. New two-point velocimetry results are presented: phase measurements show that a subtle property is shared by the three-dimensional wake and the GL model.

Two time-quasi-periodic phenomena – the second mode observed for smaller aspect ratios, and the dislocated chevron observed for larger aspect ratios – are presented and precisely related to the GL model. Only the linear characteristics of the second mode are readily explained; its existence depends on the end conditions. Moreover, through a quasi-static variation of the length, the second mode evolves continuously to end cells (and vice versa). Observations of the dislocated chevron are recalled. A very similar instability is found on the chevron solution of the GL equation, when the model parameters (c_1, c_2) move towards the phase diffusion unstable region. The early stages of this instability are qualitatively similar to the observed patterns.

1. Introduction

1.1. *Review*

A fluid of viscosity ν is forced at a steady and uniform velocity V_∞ around a circular cylinder of diameter d, the direction of the free flow being perpendicular to the axis of the cylinder. When increasing the Reynolds number $Re = V_\infty d/\nu$ above some critical value usually close to 50, a time-periodic oscillation, eventually leading to vortex shedding is observed: this is the Bénard–von Kármán instability, as it has been known for about a century. In the 1950s, Tritton (1959) noticed that in the range $70 < Re < 90$, the flow became time-quasi-periodic, he attributed the onset of a second frequency to a different regime of essentially two-dimensional shedding (see also Tritton 1971).

However, comparing Tritton's (1959) visualizations and velocity traces with work performed since then (e.g. Gerrard 1966, 1978 and Gaster 1969, 1971) leaves no doubt that he observed a three-dimensional wake, with spanwise cells oscillating at distinct frequencies and separated by vortex dislocations. In fact, even time-periodic wakes are

† Present address: Centre d'Etude de Cadarache 13108 St Paul les Durance, France.

hardly two-dimensional because the vortex lines are not parallel to the cylinder. Gerrard (1978) reported oblique shedding, consisting of straight and parallel vortices, but not in the cylinder direction, while Hama (1957) and Slaouti & Gerrard (1981) observed parenthesis-shaped vortices. Sometimes, three-dimensional vortices break, producing cells and time quasi-periodic fluctuations. The explanation of these various three-dimensional effects has motivated many papers over the past thirty years.

Gaster (1969, 1971) obtained a second frequency and bent vortices by imposing a non-uniform basic flow. He observed that a discontinuity in the frequency–velocity relation occurred when the dislocation between two cells moved across the probe. He did not prove in any way that a uniform flow should be free of quasi-periodicity: indeed, he could not get rid of the second frequency, even though the flow was apparently uniform (Gaster 1971).

Body vibrations are a quite confusing effect, which Berger (1967) treated very early, and applied to wake control. Berger & Wille (1972) reviewed numerous contradictory experiments. Sreenivasan (1985), seeking an example for some general features of transition to turbulence, observed windows of chaos in a wake. Van Atta & Gharib (1987) revealed that aero-elastic coupling was involved in his observations. Their 'measurements suggest that if there were absolutely no vibration a Strouhal–Reynolds number [frequency–velocity] plot would have absolutely no discontinuities'.

In practical situations, only a finite length L is available (L is precisely defined in §3.2). This fact was often overlooked, and the importance of the end configuration and the aspect ratio L/d was only slowly recognized. Slaouti & Gerrard (1981) 'found that the wake structure was strongly affected by the flow configuration near the ends of the body, which itself depended entirely on the constraints imposed by the end construction'. More precisely, Gerich & Eckelmann (1982) identified end cells in the cases of an end plate (with a boundary layer) and of a free end (with a pressure short circuit around the tip, increasing the base pressure).

During the 1980s, the original ideas of Landau (see Landau & Lifchitz 1971) were applied successfully to the Bénard–von Kármán instability (Mathis 1983; Mathis, Provansal & Boyer 1984*a*; Strykowski 1986; Provansal, Mathis & Boyer 1987; Provansal 1988). The Landau model allocates only two degrees of freedom to the wake, corresponding to the complex amplitude of the unique unstable mode, and proposes a simple equation for the complex amplitude.

The understanding of the instability was greatly improved by a simple observation: not too close to the body, the flow is almost parallel (to the free flow). This approach benefits from the relative simplicity of the parallel-flow stability analysis. The global stability properties of the wake were related to the local stability properties of the velocity profiles at different streamwise locations (Monkewitz 1988; Huerre & Monkewitz 1990). Some five diameters downstream from the circular cylinder, in an area called 'wave maker', local disturbances grow, leading to self-sustained oscillations: the Bénard–von Kármán instability is an absolute instability, and the Landau model is relevant.

However, the zero-dimensional Landau model is unable to explain three-dimensional or time-quasi-periodic effects. For small aspect ratios ($L/d \lesssim 20$), the most prominent effects are the dependence of the Landau model parameters – including the critical Reynolds number Re_1 – on the aspect ratio, the dependence of the oscillation amplitude on space coordinates, and the onset of a second mode (Mathis 1983; Mathis, Provansal & Boyer 1984*a*, *b*). Since 1988, many detailed and valuable observations on large aspect ratio wakes have been reported (e.g. Williamson 1988, 1989; König, Eisenlohr & Eckelmann 1990; Lee & Budwig 1991; Noack, Ohle & Eckelmann 1991;

Leweke, Provansal & Boyer 1993). In particular, for large aspect ratios ($L/d \gtrsim 20$), Williamson (1989) showed that the end effect propagated from the end along the whole span, imposing various three-dimensional effects, including a chevron pattern, without either flow non-uniformity or vibrations.

Albarède, Provansal & Boyer (1990) introduced a one-dimensional GL model, reproducing many three-dimensional effects. This model was required firstly, to be coherent with the experiments backing the Landau model (a kind of 'correspondence principle'); secondly, to represent the spanwise coupling, which seems to be the major principle of pattern selection in this problem. Similar studies were performed by Gaster (1969) (without the present mathematical and computational possibilities), Noack *et al.* (1991), Papangelou (1992), Chiffaudel (1992), with variations, like a flow profile, or a Van der Pol oscillator instead of a Landau oscillator. According to Le Dizes, Monkewitz & Huerre (1992), the GL equation can be deduced from the Navier–Stokes equations as an asymptotic expansion.

Once the GL model and some of its strikingly realistic features were revealed, a more systematic and quantitative test was undertaken. The first step was the article by Albarède & Monkewitz (1992), intentionally limited to time-periodic (asymptotic) flows, with a foray into the consequences of flow non-uniformity (specifically, the end-plate boundary layers). The second step is the present article, where time-quasi-periodic flows will be treated.

1.2. *The nature of the three-dimensional effects at low Reynolds numbers*

For a long time, the greatest theoretical interest was attached to the basically two-dimensional flow (with spanwise translational invariance). Unfortunately, not much information is available about this flow, because it does not exist in nature. However, we will sketch briefly its plausible stability characteristics.

The basically two-dimensional flow has symmetries: time translational invariance and spanwise translational invariance. The former is broken for $Re > Re_0 \approx 50$. It follows a time-periodic bifurcating flow, with only spanwise translational invariance.

For $Re \gtrsim 180$, flow visualizations (Hama 1957 and Williamson 1988) show z-periodic patterns, with a spanwise wavelength independent of the length, indicating an instability of the two-dimensional bifurcating flow. (Here, as usual, z is the spanwise coordinate, x is the streamwise coordinate, and y is defined by (x, y, z) being a direct orthogonal frame.) In the simplest case, the flow would be linearly unstable with respect to some z-sinusoidal disturbance; in reality, the sudden appearance of highly nonlinear patterns, like horseshoe vortices, and the existence of hysteresis (Williamson 1988), suggest that finite-amplitude perturbations are involved in the (subcritical) bifurcation.

We now limit the scope of our study to the flow around a finite-length body, at Reynolds numbers low enough ($Re \lesssim 180$), such that no three-dimensional instability of the two-dimensional basic flow is expected. Many complicated three-dimensional effects are nevertheless observed. Indeed, there is a conflict between the finite span and the diverging critical correlation length, which is known from the bifurcation theory of spatially extended systems (Kuramoto 1984): this results in a strong finite-length effect. For larger rescaled lengths (either larger aspect ratios or larger Reynolds numbers, within the above limit), the correlation length is much smaller than the body length and the concept of an end effect is more relevant, because the pattern does not depend on the actual length, but on the mere existence of ends, and on flow details near the ends.

2. The Ginzburg–Landau model and its properties

In this section, we recall the GL model and its simple properties, which, essentially, have already been presented, along with experimental verifications, in Albarède & Monkewitz (1992). Our aim is to give established aspects of the GL model that will be used later as a basis to treat new or more controversial issues.

2.1. *The Ginzburg–Landau model*

The wake parameters are V_∞, d, ν, L; d^2/ν and d can be used as natural time and length units (mass does not appear because we do not consider pressure). The dimensionless wake parameters are the Reynolds number and the aspect ratio.

A thin slice of the wake (for example between z and $z+\mathrm{d}z$) is a local oscillator governed by a Landau equation with a complex linear coefficient $\sigma = \sigma_r + \mathrm{i}\sigma_i$ and a complex nonlinear coefficient $l = l_r + \mathrm{i}l_i$. A diffusive coupling is added, with a complex diffusive coefficient $\mu = \mu_r + \mathrm{i}\mu_i$. In its simplest form, the model consists of the following relation:

$$v(t, x_0, y_0, z, Re) = V_{00}(x_0, y_0, Re) + \mathrm{Re}\,[A(t, z, Re)], \tag{2.1}$$

where A is a complex solution of the GL equation

$$\partial_t A = \sigma A + \mu \partial_z^2 A - l|A|^2 A, \tag{2.2}$$

and obeys the boundary conditions

$$A(t, \pm L/2) = 0. \tag{2.3}$$

We also use $M = |A|$, modulus of A.

A more realistic relationship between the complex amplitude A and the observable fields is given in the Appendix. Let 'node' denote a zero of the complex amplitude. The complex amplitude can spontaneously vanish, yielding 'free' nodes, in the interior of the definition interval. Free nodes allow phase discontinuities, and correspond physically to vortex dislocations.

The fundamental piece of information in (2.3) is the existence of nodes bound to the ends. As a first approximation, and for the experimental set-up described in §3.2, the length L used in (2.3) is the plate-to-plate distance. The consequences of this approximation are examined in §4.2.

In principle, initial conditions should be stated. However, numerical simulations show that, with small-noise conditions, i.e. small when compared to $(\sigma_r/l_r)^{1/2}$, the memory of the initial noise is usually lost after a duration of order σ_r^{-1}. Similarly, in experiments, initial conditions are usually represented by the turbulence level only.

The following quantities have been introduced: t is time, v is some (real) velocity component, V_{00} is the same component for the basic flow, (x_0, y_0) defines a measurement line, parallel to the cylinder, typically $(x_0, y_0) = (5d, d)$. In (2.2), σ, μ, l are functions of the wake parameters V_∞, d, ν only and do not depend on L, since the oscillators are only locally controlled (this might be wrong, if the conclusions of Davey, Hocking & Stewartson 1974 about shear flows were equally applicable to wakes). They can be replaced by their complex conjugates without any effect on observable quantities. Thus, we must indicate the conventional choice $\sigma_i > 0$. It affects the signs of l_i and μ_i. From dimensional considerations, $\sigma d^2/\nu$, μ/ν, $l\nu$ are functions of Re only. In particular, the correspondence with the Landau model leads to

$$\sigma_r = k(Re - Re_0). \tag{2.4}$$

Re_0 is the critical Reynolds number in the limiting case $L/d \to \infty$. We use the value of k from Mathis (1983) or Provansal *et al.* (1987):

$$k = 0.20 \pm 0.02\nu/d^2, \quad Re < 80. \tag{2.5}$$

Following Albarède & Monkewitz (1992), we use

$$Re_0 = 48.5 \pm 1.5. \tag{2.6}$$

2.2. *The linearized problem*

With the boundary conditions (2.3), we diagonalize the operator

$$(\sigma_r + i\sigma_i) + (\mu_r + i\mu_i)\,\partial_z^2$$

The eigenvalues are

$$\sigma_n = \sigma_r - \mu_r q_n^2 + i(\sigma_i - \mu_i q_n^2) \quad \text{where} \quad q_n = n\pi/L, \quad n = 1, 2, \ldots. \tag{2.7}$$

The eigenfunction associated with σ_n is

$$S_n(z) = \sin(q_n(z + L/2)). \tag{2.8}$$

The general solution of the linearized GL equation

$$\partial_t A = (\sigma_r + i\sigma_i) A + (\mu_r + i\mu_i)\,\partial_z^2 A \tag{2.9}$$

and the boundary conditions (2.3) is consequently

$$A(t, z) = \sum_{n=1,2\ldots} A_n(t)\, S_n(z). \tag{2.10}$$

A_n is called the global complex amplitude of the nth linear mode and obeys

$$\partial_t A_n = \sigma_n A_n. \tag{2.11}$$

We also use $M_n = |A_n|$, modulus of A_n.

The nth linear mode is linearly excited when the real part of σ_n is positive, which occurs for $L > n\pi(\mu_r/\sigma_r)^{1/2}$. In particular, the critical Reynolds number Re_1, found by equating the growth rate σ_{1r} to zero, is given by the relation

$$Re_1 = Re_0 + (\mu_r/k)\, q_1^2 = Re_0 + (\mu_r/k)\,(\pi/L)^2. \tag{2.12}$$

2.3. *The rescaled Ginzburg–Landau equation*

Following Kuramoto (1984), we propose new scales for amplitude, time and space, based on σ_r, μ_r and l_r:

$$\bar{A} = A(l_r/\sigma_r)^{1/2}, \quad \bar{t} = t\sigma_r, \quad \bar{z} = z(\sigma_r/\mu_r)^{1/2}. \tag{2.13}$$

The new time and space scales can be used to rescale all measured quantities. (These rescaled quantities must not be confused with dimensionless quantities, based on d^2/ν and d.) In particular, the length of the body yields a 'Kuramoto' rescaled length:

$$\bar{L} = L(\sigma_r/\mu_r)^{1/2} = L[k(Re - Re_0)/\mu_r]^{1/2}, \tag{2.14}$$

which is a function of both the Reynolds number and the aspect ratio.

The nth linear mode is linearly excited when the real part of σ_n is positive, which occurs for $\bar{L} > n\pi$ or $\bar{q}_n < 1$. The rescaled GL equation is

$$\partial_{\bar{t}} \bar{A} = (1 + ic_0)\bar{A} + (1 + ic_1)\,\partial_{\bar{z}}^2 \bar{A} - (1 + ic_2)|\bar{A}|^2 \bar{A}, \tag{2.15}$$

where $c_0 = \sigma_i/\sigma_r$, $c_1 = \mu_i/\mu_r$ and $c_2 = l_i/l_r$ are functions of the Reynolds number only.

As c_0 affects the solution only by a frequency shift, the mathematically significant model parameters are the coefficients (c_1, c_2) and the rescaled length $\bar{L}$. The critical condition for the flow oscillation is $\bar{L} = \pi$, a relation equivalent to $Re = Re_1$. As long

as the variation of the coefficients (c_1, c_2) with Re can be neglected, $\bar{L}$ alone represents the evolution of the wake when varying Re or L/d. In this sense, $\bar{L}$ is the main parameter of the wake. As a simple but striking consequence, (2.14) shows that doubling the aspect ratio (for a given Reynolds number) is equivalent to quadrupling the difference $Re - Re_0$ (for a given aspect ratio).

2.4. *The one-mode approximate solution: correspondence with the Landau model*

We limit the expansion (2.10) to the first linear mode:

$$\bar{A}(\bar{t}, \bar{z}) = \bar{A}_1(\bar{t})\, S_1(\bar{z}). \tag{2.16}$$

This truncation is roughly applicable if $\pi < \bar{L} < 2\pi$ and reduces the GL model to a Landau equation:

$$d_{\bar{t}} \bar{A}_1 = \bar{\sigma}_1 \bar{A}_1 - \tfrac{3}{4}(1 + \mathrm{i}c_2)|\bar{A}_1|^2 \bar{A}_1, \tag{2.17}$$

or, without rescaling,

$$d_t A_1 = \sigma_1 A_1 - \tfrac{3}{4}l|A_1|^2 A_1. \tag{2.18}$$

The coefficient $\frac{3}{4}$ originates from the relation $4\sin^3(x) = 3\sin(x) - \sin(3x)$. Equation (2.18) is the basis of the former Landau model. It is definitely not the Landau equation obtained from the GL equation by suppressing the z-dependence.

The asymptotic solution of (2.18) is

$$\bar{A}_1 = \bar{M}_1 \exp(\mathrm{i}\bar{\omega}_1 \bar{t}), \tag{2.19}$$

with

$$\bar{M}_1^2 = \tfrac{4}{3}(1 - \bar{q}_1^2), \tag{2.20}$$

$$\bar{\omega}_1 = c_0 - c_2 - \bar{q}_1^2(c_1 - c_2). \tag{2.21}$$

$\bar{A}(\bar{t}, \bar{z}) = \bar{A}_1(\bar{t})\, S_1(\bar{z})$ is the sum of two planes with wavenumbers $\pm\bar{q}_1$ and the angular frequency $\bar{\omega}_1$, interfering so as to obey the boundary conditions (2.3).

The 'adiabatic' elimination of the linear modes with $n > 1$ is actually not correct, because the excited first linear mode is coupled with the other linear modes with odd n (all these modes being moreover synchronized). From Albarède & Monkewitz (1992), with

$$\epsilon = (\bar{L}/\pi - 1)^{1/2}, \tag{2.22}$$

(2.20) and (2.21) should be corrected by $O(\epsilon^3)$ and $O(\epsilon^4)$, and some $O(\epsilon^2)$ spanwise phase variation must be allowed. However, as long as $\bar{L} \lesssim 3\pi$ and no second mode is observed, the Landau model is a sufficiently accurate representation of the amplitude and frequency measurements.

2.5. *The large-L approximate solution*

We consider the case $\bar{L} \gg \pi$. Physically, this can be achieved, without bound, by setting a large aspect ratio for a constant Reynolds number or by setting a large Reynolds number for a constant aspect ratio, although, in the latter case, the coefficients $(c_1, c_2)(Re)$ will probably make the GL model break down for Re large enough. For now, let us concentrate on the increase of $\bar{L}$ for constant (c_1, c_2). We also restrict our analysis to time-sinusoidal solutions, which always exist, and are often stable asymptotic solutions (they correspond to time-periodic flows).

Using rescaled quantities, a time-sinusoidal solution can be written:

$$\bar{A}(\bar{t}, \bar{z}) = \bar{M}(\bar{z}) \exp(\mathrm{i}\phi(\bar{t}, \bar{z})), \quad \bar{M} > 0, \tag{2.23}$$

$$\bar{\omega}(\bar{t}, \bar{z}) = \partial_{\bar{t}}\phi = \text{constant}. \tag{2.24}$$

ϕ is the phase; the (rescaled) angular frequency $\bar{\omega}$ is a constant, equal to $c_0 - c_2$ for parallel shedding.

In an infinite medium, the GL equation has plane wave solutions:

$$\bar{A}_{\bar{q}}(\bar{t}, \bar{z}) = (1 - \bar{q}^2)^{1/2} \exp(\mathrm{i}\bar{\omega}_{\bar{q}}\bar{t} + \mathrm{i}\bar{q}\bar{z}) \quad \text{with} \quad |\bar{q}| \leqslant 1, \tag{2.25}$$

$$\bar{\omega}_{\bar{q}} = c_0 - c_2 - \bar{q}^2(c_1 - c_2). \tag{2.26}$$

$\bar{A}_0$, a parallel plane wave, corresponds to parallel shedding, and $\bar{A}_{\bar{q}\neq 0}$, an oblique plane wave, corresponds to oblique shedding. Equation (2.26) looks like (2.21), with $\bar{q}_1$ replaced by $\bar{q}$.

Actual solutions are identical to plane waves only away from the ends, where they have to comply with the boundary conditions (2.3). The plane wave emerging from the left end $z = -L/2$ has a rescaled wavenumber $\bar{q}_\infty$, which is a function of (c_1, c_2) only; by symmetry the right end selects the opposite wavenumber. The work of Nozaki & Bekki (1984) allows determination of the analytical form of $\bar{q}_\infty(c_1, c_2)$ (in particular, $\bar{q}_\infty > 0$).

The plane waves are not superposed, but connected through a 'phase shock'.† The phase shock thickness is

$$\Delta\bar{z} = \frac{2}{\bar{q}_\infty}\frac{1+c_1 c_2}{|c_1 - c_2|}. \tag{2.27}$$

The foregoing phenomena can be observed only if the aspect ratio and the Reynolds number are such that

$$\bar{L}(Re, L/d) \gg \Delta\bar{z}(c_1, c_2). \tag{2.28}$$

Away from the ends, the phase is a solution of one autonomous equation, namely the phase diffusion equation, while the amplitude is slaved to the phase. The phase diffusion coefficient is $1 + c_1 c_2$.

3. The numerical and experimental methods

3.1. *The numerical method*

The numerical method is described in detail in Albarède (1991). It is very simple and efficient, and its principle was proposed by P. Haldenwang (1989, private communication). Equations are discretized and linearized, with a time–space mesh $(\mathrm{d}t, \mathrm{d}z)$ and errors $O(\mathrm{d}t^2 + \mathrm{d}z^2)$. Initial conditions can be set arbitrarily; unless otherwise stated, they consist of random noise of rescaled amplitude 10^{-2}. A simple flag allows either zero or periodic boundary conditions to be set. The solution for the next time step is obtained by solving the resulting tridiagonal linear system, which is elementarily performed by forward elimination and backward substitution. The code reproduces very accurately analytical solutions.

Of course, the rescaled representation improves the accuracy. The mathematically non-significant coefficient c_0 can be chosen so as to obtain a low absolute angular frequency, $|\bar{\omega}| = |\partial_t \phi|$. In this case, c_0 is said to be 'adapted': the solution varies slowly, and time steps of order $1/|\bar{\omega}|$ can be used. From experiments, we know that three-dimensional effects result in frequencies only slightly (typically 20%) lower than the parallel oscillation frequency: this feature is reproduced by multiplying the numerical solution by $\exp(\mathrm{i}\Delta c_0 t)$, where $c_0 + \Delta c_0$ should be the rescaled physical linear angular frequency. Actually, we use a much lower Δc_0, in order to introduce a stroboscopic slowing down, helpful for visualization (see figure 14*a*, etc.).

3.2. *The experimental method*

The apparatus should allow a continuous and independent variation of the dimensionless wake parameters $(Re, L/d)$, in order to observe the birth, evolution and interaction of the different modes involved. This was not the case with the old

† A term sanctioned by use, but slightly misleading, since the solution is infinitely smooth.

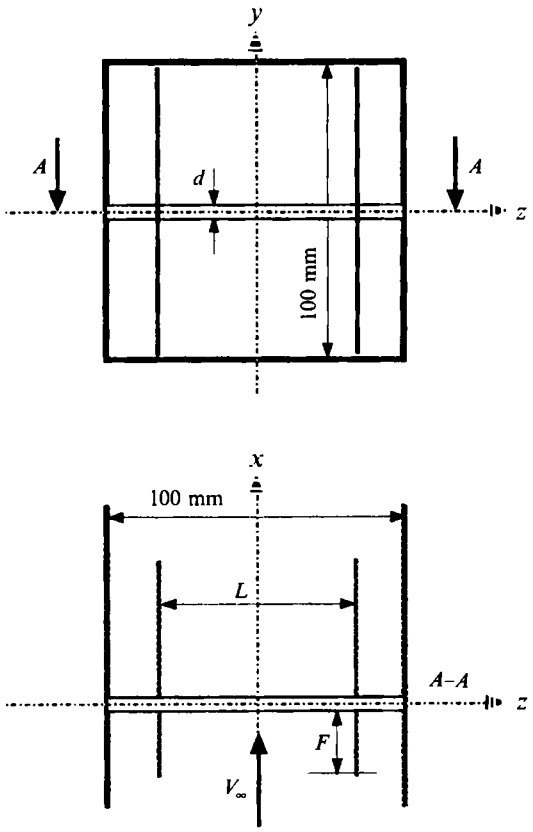

FIGURE 1. The wind tunnel and the obstacle, fitted with end plates. New apparatus: $d = 1.6$ mm, $F = 20$ mm. Old apparatus: variable d, constant $L = 100$ mm, no end plates.

apparatus used at LRC: L/d was varied by using rods with different diameters and identical lengths, which also required an adjustment of the upstream velocity to keep the Reynolds number unchanged. Even so, there were necessarily violations of hydrodynamic similarity (boundary layers, blockage effect, etc.).

The effect of the aspect ratio variation was revealed more clearly with a new apparatus, with mobile end plates and a constant diameter $d = 1.6$ mm (see figure 1). The overall mechanical set up fulfilled the symmetry $z \rightarrow -z$. The end plates were ideally half-planes defined by ($x > -F$ and $z = \pm L/2$) with a fetch $F = 20$ mm. With the old apparatus, the end plates were wind tunnel walls, with $F \approx 15$ cm. The fetch is a wake parameter. More generally, the end condition can be represented by a set of parameters. (Small sets are obtained for simple geometries, such as free ends, disk or plane end plates, etc.)

The wind tunnel had a 16 to 1 contraction, ending into a 10 cm square section. The upstream flow was regulated by a sonic throat and calibrated by laser Doppler anemometry (LDA). The rods were stiff aluminium rods, that could not be distorted by the air flow, screwed at both ends to the Plexiglas walls. Careful attention was paid to reducing three-dimensional effects not due to the body. The velocity profile was flat ($\pm 0.5\%$) in the central part (7 cm) of the test section. In optimal conditions, the noise level, including the measurement noise, was 1% (standard deviation).

A single, mobile LDA measurement point was used to measure the free flow velocity or the streamwise velocity component (not simultaneously). Pressure was not

measured. The frequency and the amplitude (of the fundamental harmonic) were extracted from the power spectrum. A stationary hot wire was used as a second measurement probe. Average phase differences were deduced from the cross-correlation spectrum.

A very common experimental task is the measurement of a critical wake parameter, for a given mode. Two methods are available: detecting the presence of a peak in the power spectrum, above the noise level; or extrapolating the peak height to zero, following a certain theoretical or empirical law (for example (2.20)). Unless otherwise stated, we use the first method, which is quicker, although noise-level dependent. The resulting relative bias is roughly equal to the noise level itself, i.e. less than 1 % (usually negligible).

The GL model parameters are $\bar{L}$ and the coefficients σ_r, μ_r, l_r, c_0, c_1, c_2. They depend globally on the wake parameters $(Re, L/d)$. The model parameters are determined by identification of the model solutions with the measured flow. The parameters σ_r, l_r, c_0, c_2 are assumed to be provided by the previous Landau analysis. The coefficient c_0 affects the solution only by a frequency shift, and can be deduced from parallel shedding frequency measurements. In addition to the Landau model parameters, the GL model involves three parameters: $\bar{L}(Re, L/d)$, $\mu_r(Re)$, $c_1(Re)$. The variation of (c_1, c_2) as a function of Re was not precisely determined, because of the very high accuracy and great stability required. Experiments with variable L and constant V_∞, d are not affected by the variation of coefficients with Re: they can be interpreted more safely than experiments with variable V_∞ and constant L, d.

The streamwise evolution of the wake is not directly treated by the GL model. As a matter of principle, only the dominant, pattern-selecting, spanwise evolution is treated. Similarly, systematic time-dependent velocity measurements are carried out only on a spanwise segment located in the wave-making area. However, we would like to interpret smoke or dye concentration photographs of an (x, z)-plane, whereas the solution of the GL model can be compared directly only with a cinematographic recording, made on a spanwise line, or the signals of a set of hot wires located along the span (a system used by Gerrard 1966).

We assume that the smoke filaments are carried away by the flow without distortion, as if imprinted onto a solid support moving away with a celerity $c \lesssim V_\infty$. By analogy, we will call this hypothesis the 'plotter principle'. Thus a constant-time, variable-x visualization, and a variable-time, constant-x recording would correspond to each other through the simple transformation $t = -x/c$. Actually, the plotted principle is a fairly correct approximation, because a given smoke filament is carried out of observation window before being distorted much (the advection time is much shorter than the distortion time).

4. The one-mode regime

4.1. *The nonlinear Landau coefficient c_2*

Strykowski (1986) found $c_2 = -3.0$, while Provansal *et al.* (1987) found $c_2 = 0$. Since then, other evaluations have confirmed Strykowski's result:

Schumm, Berger & Monkewitz (1994):	$c_2 = -2.90 \pm 0.45$	$Re < 60$,
Noack & Eckelmann (1991):	$c_2 = -1.5$	$Re < 60$,
Dušek, Le Gal & Fraunié (1994):	$c_2 = -2.7$	$Re = 48$.

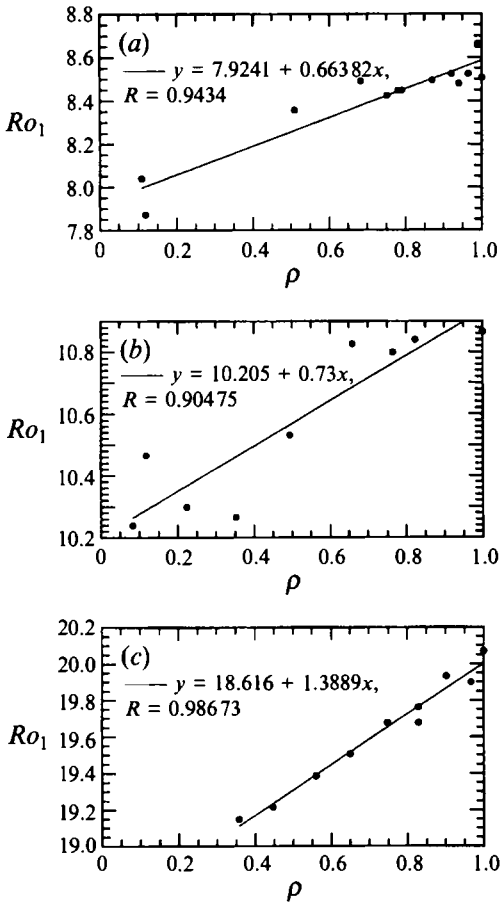

FIGURE 2. Relationship between the saturation ratio ρ (proportional to the squared amplitude) and the Roshko number Ro_1 (dimensionless frequency), during transients of the first mode, following an instantaneous shift of the free flow velocity. The wake parameters are listed in table 1, for the three cases *a*, *b*, *c*. Old apparatus used.

L (cm)	d (cm)	Re_1	$Re-Re_1$	$dRo_1/d\rho$	c_2	Figure number
10	0.6	58	6.5	0.663	−3.2	2(*a*)
10	1.0	68	8.0	0.73	−2.9	2(*b*)
10	1.6	102	22.6	1.389	−1.9	2(*c*)

TABLE 1. Experimental conditions and results

The value of Dusĕk *et al.* (1994) results from a numerical simulation of the Navier–Stokes equations. There are still large discrepancies between these results, and the determination of c_2 is still an open problem.

A reliable measurement of c_2 results from recording the squared amplitude and frequency during transients following an instantaneous shift of the free flow velocity (while the other wake parameters are steady). The solution of the Landau equation (2.18), without assuming a steady angular frequency, yields a linear relation between

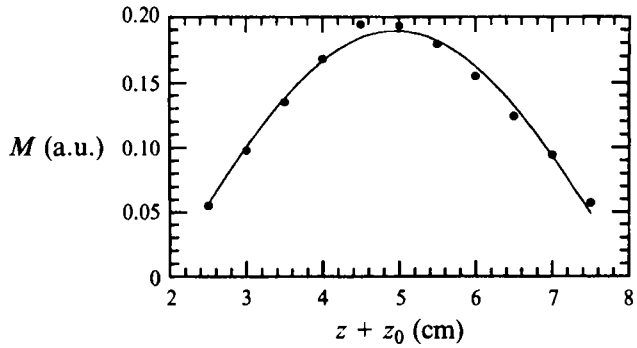

FIGURE 3. Spanwise variation of the first-mode amplitude M. Wake parameters: $Re = 58.8$, $L = 76$ mm, $d = 4$ mm, $F = 10$ mm. Fitting formula: $M(Z) = M_1 \cos(\pi(Z - z_0)/L')$ (where $Z = z + z_0$). Result: wake centre $z_0 = 49.6$ mm, influential length $L' = 60.6$ mm, amplitude $M_1 = 0.189$ arbitrary units (correlation 0.993).

the time-dependent angular frequency (time-derivative of the phase) and the saturation ratio, $\rho(t) = [M_1(t)/M_1]^2$, such that $\lim_{t\to\infty} \rho = 1$:

$$\omega_1(t) = 2\pi f_1(t) = \sigma_{1i} - c_2 \sigma_{1r} \rho = \sigma_{1i} - c_2 k(Re - Re_1)\rho(t). \tag{4.1}$$

We present three experiments (see figure 2*a–c*) using the old apparatus: the relation (4.1) is acceptable and leads to values of c_2 according to

$$c_2 = (2\pi/k)(Re - Re_1)^{-1} \mathrm{d}f_1/\mathrm{d}\rho \approx 10\pi(Re - Re_1)^{-1}(\mathrm{d}Ro_1/\mathrm{d}\rho). \tag{4.2}$$

Ro, the Roshko number, is a common notation for a dimensionless frequency: $Ro = fd^2/\nu$. Experimental conditions and results are collected in table 1. From these results, we keep for further use in this paper

$$c_2 = -2.6 \pm 0.7 \quad \text{for} \quad Re < 100. \tag{4.3}$$

4.2. *The determination of the Ginzburg–Landau diffusion coefficient* μ

4.2.1. *The dissipative real part* μ_r

The initial evaluation of μ_r by Albarède & Monkewitz (1992),

$$\mu_r = 32 \pm 6\nu, \quad Re < 100, \tag{4.4}$$

is based on (2.12), where L is the plate-to-plate distance. Two remarks can be made about this method of evaluation. First, the values of μ_r obtained by Albarède (1991) from various experiments, with different end plate configurations and Reynolds number ranges, are somewhat scattered, from $\mu_r = 24\nu$ to 39ν, and the scattering is larger than the fit accuracy. Secondly, in (2.3), the bound notes are wrongly assumed to be located on the end plates. Although the nodes are indeed quite close to the end plates, this assumption is not quantitatively correct.

Let us propose a more careful application of the zero boundary conditions:

$$A(t, \pm L'/2) = 0, \tag{4.5}$$

where $z = \pm L'/2$ is the actual position of the nodes. In practice (see figure 3 for example), the experimental spanwise variation of the first mode amplitude is fitted with a sinusoid and the nodes are obtained by intersecting the sinusoid with the z-axis. The 'influential' length L' is smaller than the plate-to-plate distance L, because of partly subcritical end-plate boundary layers. (Gerich & Eckelmann 1982 measured very carefully node-to-plate distances, but only for large-$\bar{L}$ flows.)

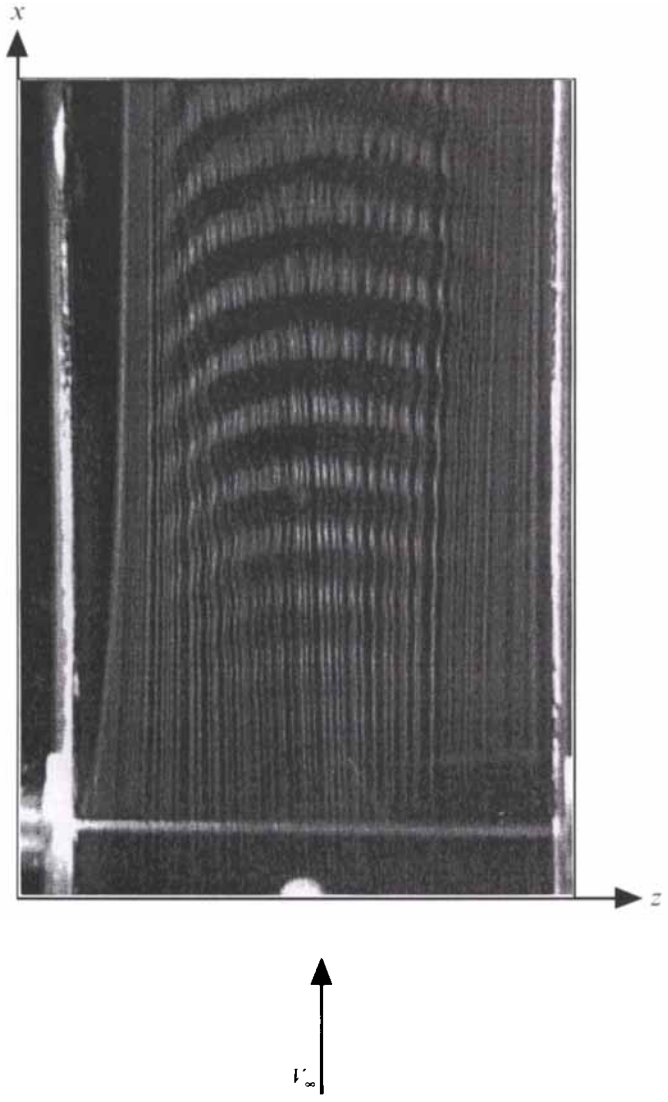

FIGURE 4. Visualization of the first mode (courtesy of T. Leweke): $Re = 50$, $L = 75$ mm, $d = 1.3$ mm, $\bar{L} = 1.9\pi$.

The results of §2 are applied with the notation changes $L \to L'$, $\mu \to \mu'$, where μ' is the actual GL diffusion coefficient. In particular, (2.3), (2.12) and (2.13) become

$$\partial_t A = \sigma A + \mu' \partial_z^2 A - l|A|^2 A, \tag{4.6}$$

$$Re_1 = Re_0 + (\mu_r'/k)(\pi/L')^2, \tag{4.7}$$

$$\bar{A} = A(l_r/\sigma_r)^{1/2}, \quad \bar{t} = t\sigma_r, \quad \bar{z} = z(\sigma_r/\mu_r')^{1/2}. \tag{4.8}$$

Combining (2.12) (which becomes only a definition of μ_r) and (4.7), we obtain

$$\mu_r'/\mu_r = (L'/L)^2. \tag{4.9}$$

One must be aware that μ/ν or L'/L are (not simple) functions of Re, L/d and F/d, whereas μ'/ν is a function of Re only. In particular instances, we measured $L'/L = 0.8$ (see figure 3) and even $L'/L = 0.5$ ($Re = 52$, $L = 50$ mm, $d = 1.5$ mm, $F = 10$ mm,

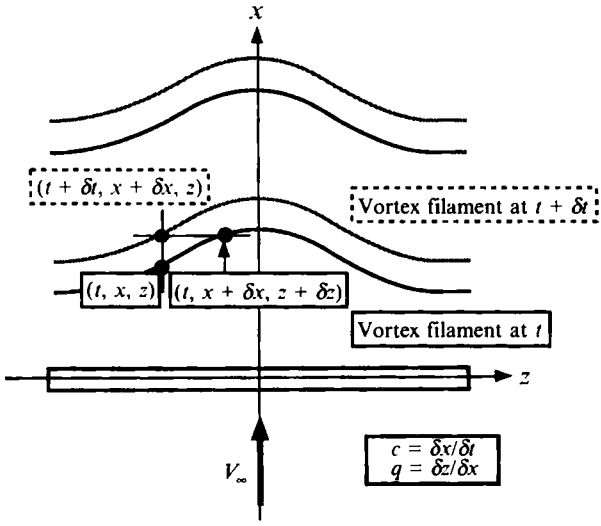

FIGURE 5. Sketch of the time and space evolution of the one-mode wake. Vortex filaments are particular isophases.

$L' = 27.5$ mm). These observations suggest $8 < \mu_r'/\nu < 21$, assuming $24 < \mu_r/\nu < 32$ (for small-F experiments). More precisely, the results of Leweke & Provansal (1994) on the torus allow the following evaluation:

$$\mu_r' = 10 \pm 4\nu \quad \text{for} \quad Re < 100. \tag{4.10}$$

The fundamental quantity is of course μ_r'. However, we often deal with small-L experiments where only L (not L') is known: in this case, μ_r must be used. For large-L experiments, $L' \approx L$ and μ_r' must be used (in particular the Kuramoto lengthscale is based on μ_r'). Of course, we recommend the systematic use of L' for future work, if a greater consistency and accuracy of the GL model is sought.

4.2.2. *The dispersive imaginary part μ_i*

Whenever necessary, we will use the following values (unaffected by the above problem), derived as in Albarède & Monkewitz (1992):

$$c_1 - c_2 = 2.7 \pm 0.6, \quad Re = 55; \tag{4.11}$$

$$c_1 = 0.1 \pm 1, \quad Re = 55. \tag{4.12}$$

Evaluation (4.12) is consistent with evaluations (4.3) and (4.11), and c_1 happens to be close to zero, although we know no theoretical reason why it should be exactly zero.

4.3. *The spanwise variation of the phase*

According to (2.19), no spanwise variation of the phase is allowed (parallel shedding). Actually, this result is true only in the limiting case $\bar{L} \to \pi$ (see §2.4). Above the threshold, the spatial Fourier coefficients of the phase can be expanded in powers of ϵ (Albarède & Monkewitz 1992), and the leading term yields

$$\phi(t, z) = (-\phi_{22})(\bar{L}/\pi - 1)(\bar{L}/2\pi)\cos(2\pi z/L) + \omega t, \tag{4.13}$$

where ϕ_{22} is defined by

$$-\phi_{22} = (c_1 - c_2)/[3(1 + c_1^2)]. \tag{4.14}$$

The sign of the phase is not arbitrary. In particular, one can check that (4.13) does predict the correct curvature for vortices, as seen in figure 4 or figure 5 (for this

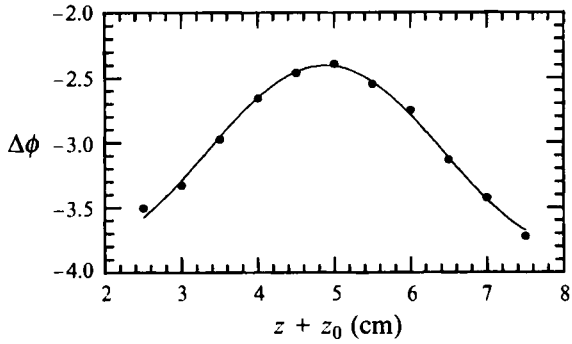

FIGURE 6. Spanwise variation of the phase. Same wake parameters as those of figure 3. Fitting formula: $\Delta\phi(Z) = (\phi_{pp}/2)\cos(2\pi(Z-z_0)/L')+\Delta\phi_m$ (where $Z = z+z_0$). Result: z-average phase difference $\Delta\phi_m = -3.08$, wake centre $z_0 = 48.8$ mm, influential length $L' = 62.9$ mm, $\phi_{pp} = 1.36$ (correlation 0.997).

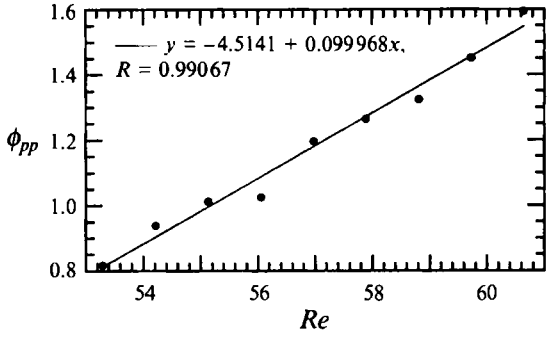

FIGURE 7. ϕ_{pp} (peak to peak spanwise variation of the phase) *vs.* the Reynolds number. Same wake parameters as those of figure 3.

purpose, one needs the following elements: $-\phi_{22} > 0$, which is clear from (4.11); $\omega > 0$, which results from the sign convention on σ_i made in §2.1, and the plotter principle of §3.2) The comparison can be made more quantitative, by measuring (as in figure 6) the spanwise variation of the phase, defined as $\Delta\phi(z) = \phi(t,z)-\phi(t,0)$. Data are fitted with the formula

$$\Delta\phi(z) = (\phi_{pp}/2)\cos(2\pi z/L')+\Delta\phi_m. \tag{4.15}$$

The fit parameters are the peak to peak value ϕ_{pp}, the constant $\Delta\phi_m$ and the influential length L'.

In an experiment with variable V_∞ and constant L, d, we observe that ϕ_{pp} varies linearly with Re. From (4.13) and (4.15), we easily derive

$$-\phi_{22} = 2(Re_1 - Re_0)\partial_{Re}\phi_{pp}(Re_1). \tag{4.16}$$

From figure 7, (2.12) and evaluation (4.4), we obtain $\partial_{Re}\phi_{pp} = 0.100$, $L = 76$ mm, $d = 4$ mm, $Re_1 - Re_0 = 4.4 \pm 0.9$ and finally $-\phi_{22} = 0.9 \pm 0.2$. From evaluations (4.3), (4.11) and equation (4.14), we obtain $-\phi_{22} = 0.8 \pm 0.3$. The amplitude (and shape) of the phase variation are thus quantitatively predicted. We also obtain a fairly sensitive measurement of ϕ_{22}.

We also performed an experiment with variable L and constant V_∞, d: ϕ_{pp} increases linearly with $\bar{L}$, and the resulting estimate of $-\phi_{22}$ is compatible with the above values.

5. The second mode

5.1. *The existence and the critical Reynolds number of the second mode*

A second mode (figure 8) is observed when the Reynolds number is increased above a critical value $Re_2 > Re_1$ (Mathis 1983; Mathis, *et al.* 1984*a*, *b*). It is characterized by the presence of a second frequency f_2 in the spectrum of the velocity fluctuations. We will show that this second mode near its threshold is the second linear mode.

We begin by checking whether the critical Reynolds number Re_2 follows the linear theory critical relation

$$0 = \sigma_{2r} = k(Re_2 - Re_0) - \mu_r q_2^2. \tag{5.1}$$

A first set of data is obtained from experiments with the old apparatus: with the data of Mathis (1983), Re_2 is plotted as a function of $q_2^2 = (2\pi/L)^2$ (see figure 9). The fit with (5.1) yields $\mu_r = 42\nu$ and $Re_0 = 48.7$, fairly close to $\mu_r = 39\nu$ and $Re_0 = 49.7$ obtained likewise for the first mode (Albarède 1991).

A second set of data is obtained from experiments with the new apparatus. We have to check that the critical length of the second mode (2π) is twice that of the first mode (π), for any given Reynolds number. More generally, we check in figure 10 whether the wake parameters $(Re, L/d)$ for miscellaneous critical configurations obey the critical relations

$$Re_n = Re_0 + (\mu_r/k)\, q_n^2 \quad \text{for} \quad n = 1, 2. \tag{5.2}$$

With the new apparatus only, the second mode is not observable for $Re < Re_c$, where

$$Re_c = 57, \tag{5.3}$$

even if $\bar{L}$ is increased up to 3π (this appears in figure 7 of Albarède & Monkewitz 1992, where q_1^2 reaches nearly ten times its critical value, with no onset of the second mode). The new apparatus has a much smaller fetch F than the old apparatus, hence thinner end-plate boundary layers. We will explain the role of end-plate boundary layers in the suppression of the second mode.

With the old apparatus, the fetch was $F \approx 15$ cm; for a constant length $L = 100$ mm equal to the wind tunnel width and a diameter $d = 1.6$ mm, the second mode could be observed for Reynolds numbers as low as 50. With the new apparatus, the fetch was $F = 20$ mm; for a variable length, lower than 7 cm, and a diameter $d = 1.6$ mm, the second mode could not be observed for $Re < Re_c$. The (laminar) end-plate boundary layer thickness δ obeys Blasius' law, which can be expressed adequately here as

$$\delta/d \approx 5(F/d)^{1/2}\, Re^{-1/2} \tag{5.4}$$

or, after rescaling according to (4.8),

$$\bar{\delta}(Re, F/d) \approx [5(F/d)(1 - Re_0/Re)/(\mu_r'/\nu)]^{1/2}. \tag{5.5}$$

Unlike δ, $\bar{\delta}$ increases with Re: the rescaled boundary layers are thicker, for greater Reynolds numbers. A plausible explanation of the absence of the second mode for $Re < Re_c$ is that the end-plate boundary layer supports a cell when $\bar{\delta}$ exceeds a critical value $\bar{\delta}_c$. This critical condition is inspired by the critical condition $\bar{L} > \pi$, which has been demonstrated for the first mode. As an indication, from (5.5) and known quantities, we obtain $\bar{\delta}_c = \bar{\delta}(Re_c, F/d) \approx 1$. If F/d were small enough, there might be no second mode at any Reynolds number.

5.2. *The spanwise variations of the second mode amplitude and phase*

The spanwise variation of the second mode amplitude is reported by Mathis *et al.* Boyer (1984*b*), and the result is closely similar to the theoretical expectation.

A prominent feature of the second linear mode is the change of sign of $S_2(z)$ (or the

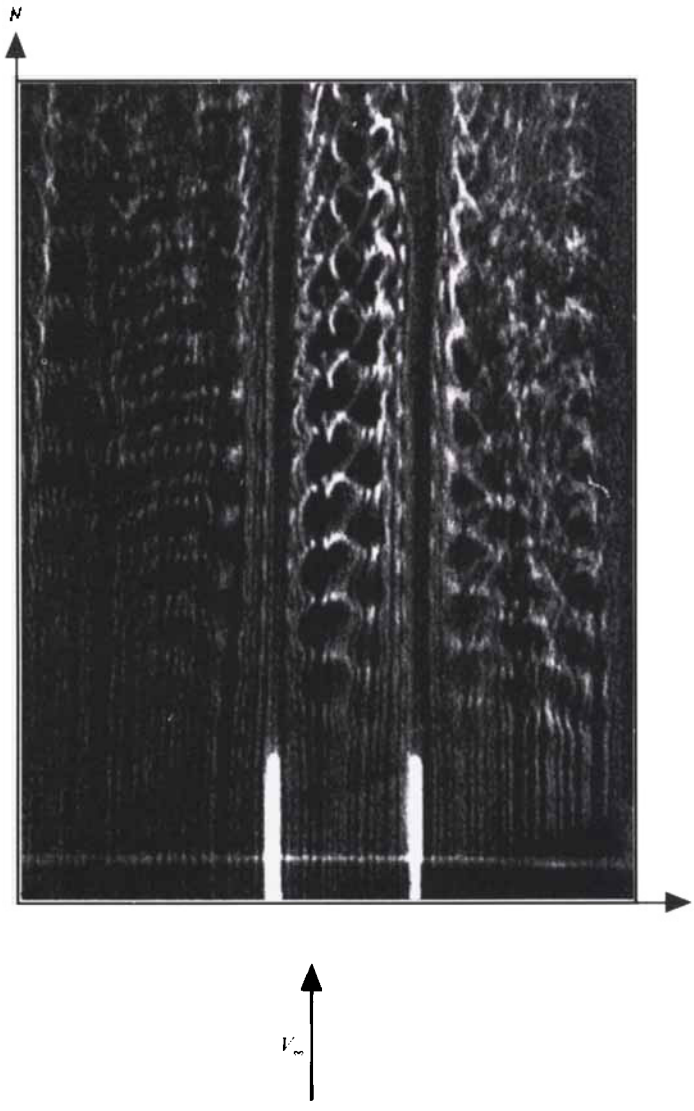

FIGURE 8. Visualization of isophase vortex lines in the second-mode regime, using the smoke wire method (courtesy of T. Leweke): $Re = 95$, $L = 21$ mm, $d = 1.3$ mm, $L/d = 16$, $\bar{L} = 2.9\pi$.

π phase jump) at $z = 0$, corresponding to a dislocation with phase opposition at midspan. Gerich (1987) published a flow photograph showing phase opposition for all x, and confirmed phase opposition also for all t (Gerich 1990, private communication). His figure c shows the second mode, in experimental conditions corresponding to a rescaled length $\bar{L} \approx 3.5\pi$. His figure d shows the first mode, with $\bar{L} \approx 2.2\pi$, which is still compatible with the condition for the one-mode regime ($\bar{L} < 2\pi$), if some uncertainty is allowed.

This interpretation is fully confirmed by flow visualization in our wind tunnel (Provansal, Leweke & Albarède 1992 or Albarède, Leweke & Provansal 1992), where we can determine more accurately the model parameters. When $\bar{L} > 2\pi$, a phase opposition is clearly observed between the left (negative z) and right (positive z) parts of the wake (see figure 8). When $\bar{L} < 2\pi$, only the first mode is observed (see figure 4).

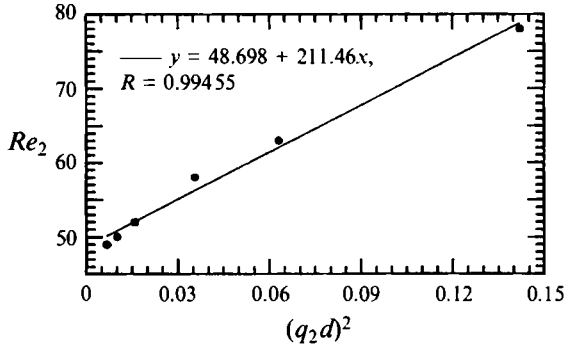

FIGURE 9. Second-mode critical Reynolds numbers Re_2 *vs.* $(q_2 d)^2 = (2\pi d/L)^2$. Data from Mathis (1983) (non-corrected values). Old apparatus used.

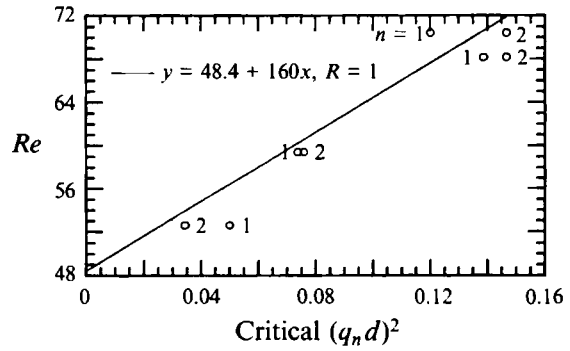

FIGURE 10. Reynolds number *vs.* critical $(q_n d)^2 = (n\pi d/L)^2$ of the nth mode ($n = 1, 2$). According to the GL model (and evaluation (4.4)), all points should lie on the straight line. We gathered miscellaneous experimental results, and the thresholds were determined by observing the appearance of a new frequency while varying the length. New apparatus used.

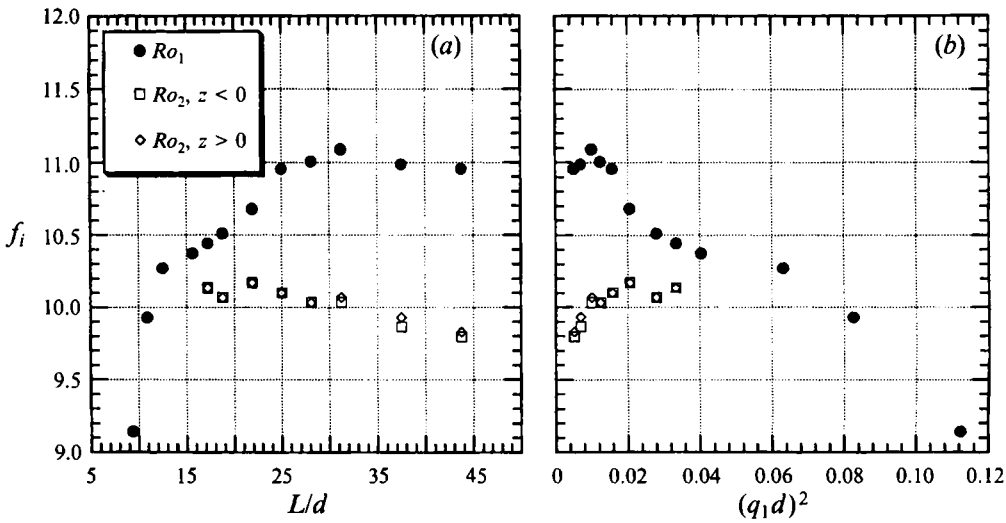

FIGURE 11. Frequencies of the first and second modes f_1 and f_2 *vs.* (*a*) L/d, (*b*) $(q_1 d)^2 = (\pi d/L)^2$, for various Roshko numbers: $Ro_n = f_n d^2/\nu$ ($n = 1, 2$). $Re = 70$. New apparatus used. For $L/d > 30$, the second mode splits into incoherent end cells. The experiment cannot be performed for $L/d > 45$ because the wind-tunnel boundary layers interfere.

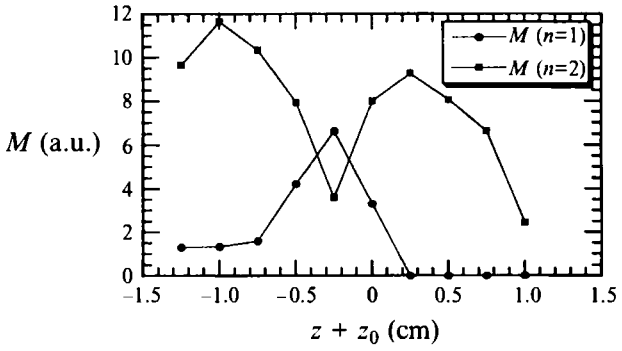

FIGURE 12. Spanwise variation of the amplitude of the first ($n = 1$) and second modes ($n = 2$), $Re = 70$, $\bar{L} = 2.6\pi$. New apparatus used.

In some cases, the left and right cells of the second mode oscillate at slightly different frequencies. Quite surprisingly, we still observe an (average) phase opposition. In fact, phase opposition is now the most frequent phase relation: once in a while (at the beat frequency), the cell with a slightly greater frequency emits an excess vortex, resulting in a swift phase jump, as observed by Mathis (1983). This behaviour results from the inevitable small dissymetry of the free flow.

5.3. *The influence of the aspect ratio on the second mode*

At $Re = 70$, we measured the variation of the frequency with L (figure 11 *a*, *b*). The global amplitude of the second mode increases quickly with the length, and for $\bar{L} = 2.6\pi$, it is already greater than the global amplitude of the first mode (see figure 12). This explains why only the second mode appears on visualizations (figure 8 and Gerich 1987, figure *c*). Phase opposition was not checked, because only one probe was available; but the right and left frequencies were rigorously identical; otherwise, we would have detected the characteristic low-frequency beat.

For $\bar{L} \approx 3\pi$, the second mode splits into end cells, with slightly different frequencies f_2 and f_2' (implying a small dissymetry). Then, the wake exhibits the nonlinear mixing of three frequencies (f_1, f_2, f_2'), with in particular the characteristic low-frequency beat at $|f_2 - f_2'|$ (Albarède 1989).

For even greater $\bar{L}$, we know, from Gerich & Ekelmann (1982), that the first mode regains spatial predominance, away from the ends. The end cells are well separated, do not interact and are independent of the length: the finite-length effect, through a nonlinear saturation process has been replaced by an end effect. Gerich & Eckelmann (1982) had shown that the end cells are linked to the end-plate boundary layers. We have shown that they are linked to the second mode through the variation of $\bar{L}$. Thus, by transitivity, the second mode is linked to the end-plate boundary layers. The end-plate boundary layers enhance the second mode or end cells, both of them being different limits of a single mode with odd parity.

5.4. *Analysis of the second mode within the GL model*

It is very important to examine if the GL model can also explain the nonlinear properties of the second mode (the saturated amplitude, and the distortion of the shape). For this purpose, we use the mode expansion (2.10), truncated to the first and second linear modes:

$$\bar{A}(\bar{t}, \bar{z}) = \bar{A}_1(\bar{t})\, S_1(\bar{z}) + \bar{A}_2(\bar{t})\, S_2(\bar{z}). \tag{5.6}$$

This truncation is roughly applicable if $2\pi < \bar{L} < 3\pi$ and reduces the GL model to a set of nonlinear differential equations (the superscript * is used for complex conjugates):

$$d_{\bar{t}}\bar{A}_1 = \bar{\sigma}_1\bar{A}_1 - (1+\mathrm{i}c_2)(\tfrac{3}{4}|\bar{A}_1|^2\bar{A}_1 + \tfrac{1}{2}\bar{A}_1^*\bar{A}_2^2 + \bar{A}_1|\bar{A}_2|^2), \tag{5.7}$$

$$d_{\bar{t}}\bar{A}_2 = \bar{\sigma}_2\bar{A}_2 - (1+\mathrm{i}c_2)(\tfrac{3}{4}|\bar{A}_2|^2\bar{A}_2 + \tfrac{1}{2}\bar{A}_2^*\bar{A}_1^2 + \bar{A}_2|\bar{A}_1|^2). \tag{5.8}$$

These coupled equations have no solution $(\bar{M}_1\exp(\mathrm{i}\bar{\omega}_1\bar{t}+\phi_1)), M_2\exp(\mathrm{i}(\bar{\omega}_2\bar{t}+\phi_2)))$, with constant $\bar{M}_n, \bar{\omega}_n, \phi_n$ $(n = 1, 2)$ and $\bar{\omega}_1 \neq \bar{\omega}_2$, unless $\bar{M}_1 = 0$ or $\bar{M}_2 = 0$.

In the numerical simulation of the GL equation for $2\pi < \bar{L} < 3\pi$ and random noise initial conditions, the second mode does not appear. When imposed in the initial conditions with a small rescaled global amplitude $\bar{M}_2 = 10^{-2}$, it does grow according to the linear theory, up to a certain time, when it is suddenly overwhelmed and annihilated by the first mode. The first mode starts at a very low level on the numerical noise, but, as it grows faster ($\sigma_{1r} > \sigma_{2r}$), it is eventually stronger than, and able to exclude, the second mode. We call this phenomenon 'nonlinear damping'.

We tried without success to trigger the second mode by introducing boundary layers in the numerical velocity profile (for $\bar{L} \gtrsim 2\pi$). In fact, the link between the second mode and the end configuration might escape the GL model because the weakly three-dimensional approximation completely breaks down near the ends: there, the flow is not weakly three-dimensional, the wake is unrelated, even locally, to the plane wake, and the stability properties can hardly be represented by $\mathrm{Re}(z)$ and a one-dimensional model.

6. The description of large-$\bar{L}$ flows by the GL model

We consider wakes obeying the relation (2.28), for example $\bar{L} > 10\pi$, where the rescaled length $\bar{L}$ is defined by (2.14). Since the Reynolds number cannot be too large, the aspect ratio cannot be too small ($Re \lesssim 180$ and $L/d \gtrsim 20$). Moreover, the Reynolds number cannot be too small (otherwise, the description of §4 is relevant).

We discuss the case of large-$\bar{L}$ flows in the stable case, when the vortex pattern consists of smoothly connected plane waves. We show that the chevron solution of the GL model becomes unstable for some values of the model parameters (c_1, c_2), and we relate this instability to experimental observations.

6.1. *The description of stable large-L flows by the GL model*

The GL model and the plotter principle have been used to interpret large-$\bar{L}$ experiments (Albarède & Monkewitz 1992). All mathematical aspects presented in §2.5 are confirmed. Empirical laws proposed by Williamson (1989), i.e. the 'cosine law' and the reflection symmetry of the phase shock in the (x, z)-plane are equivalent, as shown in Albarède (1991), to the simple relation

$$\lambda_0^2 f_0/(4\pi) = \mu_r'(c_1 - c_2), \tag{6.1}$$

where λ_0 and f_0 are the streamwise wavelength and the frequency of parallel shedding. Following §4.2, μ_r' (not μ_r) must be used in (6.1). The left-hand side of (6.1), deduced from Williamson's (1989) measurements, is well represented by the linear fit

$$\lambda_0^2 f_0/(4\pi) = 24.1 + 0.264(Re - Re_0) \quad \text{for} \quad Re < 160. \tag{6.2}$$

The right-hand side of (6.1) results from evaluations (4.3), (4.10) and (4.11). Equation (6.1) is well verified (at $Re = 55$). Similar results were obtained for the torus by Leweke & Provansal (1994). The study of the phase shock velocities, as in Albarède & Monkewitz (1992), shows a quantitative agreement with the GL model and evaluations (4.10) and (4.11).

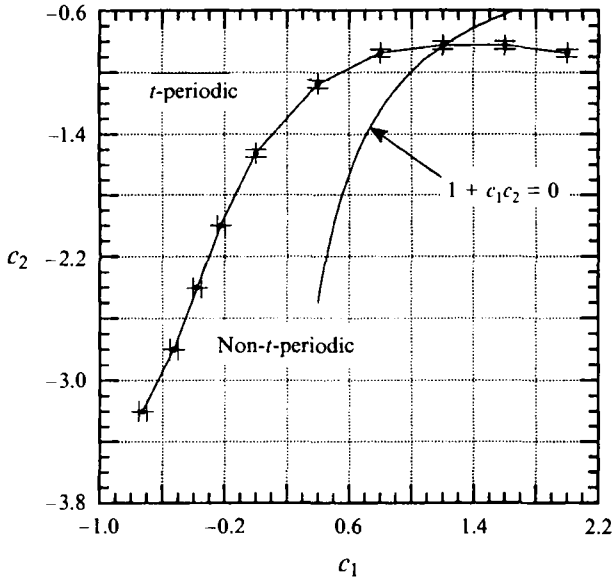

FIGURE 13. Stability diagram in the plane (c_1, c_2). In the stable (time-periodic) region, the large-$\bar{L}$ asymptotic solution is the stable chevron. In the unstable region, the following time-quasi-periodic or chaotic patterns are observed: the oscillating chevron, the dislocated chevron, the split wake. The boundary is drawn from the numerical parameters: $\bar{L} = 48$, c_0 adapted, $\mathrm{d}\bar{t} = 0.4$, $\mathrm{d}\bar{z} = 1$. The boundary of the phase-diffusion unstable region is also drawn.

The rescaled spanwise wavenumber $\bar{q}_\infty(c_1, c_2)$ can be deduced from Williamson's (1989) angle and streamwise wavelength measurements (Albarède 1991). Following §4.2, μ_r' (not μ_r) must be used for rescaling. At $Re = 64$, the experimental value of $\bar{q}_\infty$ is 0.5 ± 0.1. It is compatible with the theoretical value (see §2.5), based on evaluations (4.3), (4.10) and (4.11). The strong decrease of the experimental value of $\bar{q}_\infty$ with Re can be explained by a decrease of c_1 or an increase of c_2 (the latter was already suggested in §4.1).

6.2. *Numerical observations of large-$\bar{L}$ unstable cases (guided by experiments)*

From Williamson (1989) and König *et al.* (1990), the (time-periodic) chevron is stable only for $Re > Re_W$, with

$$Re_W = 64. \tag{6.3}$$

For $Re < Re_W$, a dislocated chevron is observed, consisting of a central cell and two lateral cells (and ever-present end cells). The central cell oscillates with a higher frequency and a lower angle.

Ideally, we consider the stability of the chevron solution with respect to variations of (c_1, c_2), for arbitrarily large $\bar{L}$. In the (c_1, c_2)-plane, we define a stable region, producing a time-periodic asymptotic solution (the usual chevron solution) for all $\bar{L}$. On the other hand, the unstable region produces non-time-periodic asymptotic solutions, for some $\bar{L}$. In practice, the stability can be investigated for a given $\bar{L}$ (here $\bar{L} = 48$), and the boundary stability will hopefully not depend much on $\bar{L}$ (the dependence of the unstable solution on $\bar{L}$ will be treated separately). A simple approximate stability condition, found numerically, is

$$\bar{q}_\infty(c_1, c_2) < 0.55. \tag{6.4}$$

The stability diagram appears in figure 13 (see also Albarède & Monkewitz 1992).

The instabilities observed in experiments and in the GL model are essentially

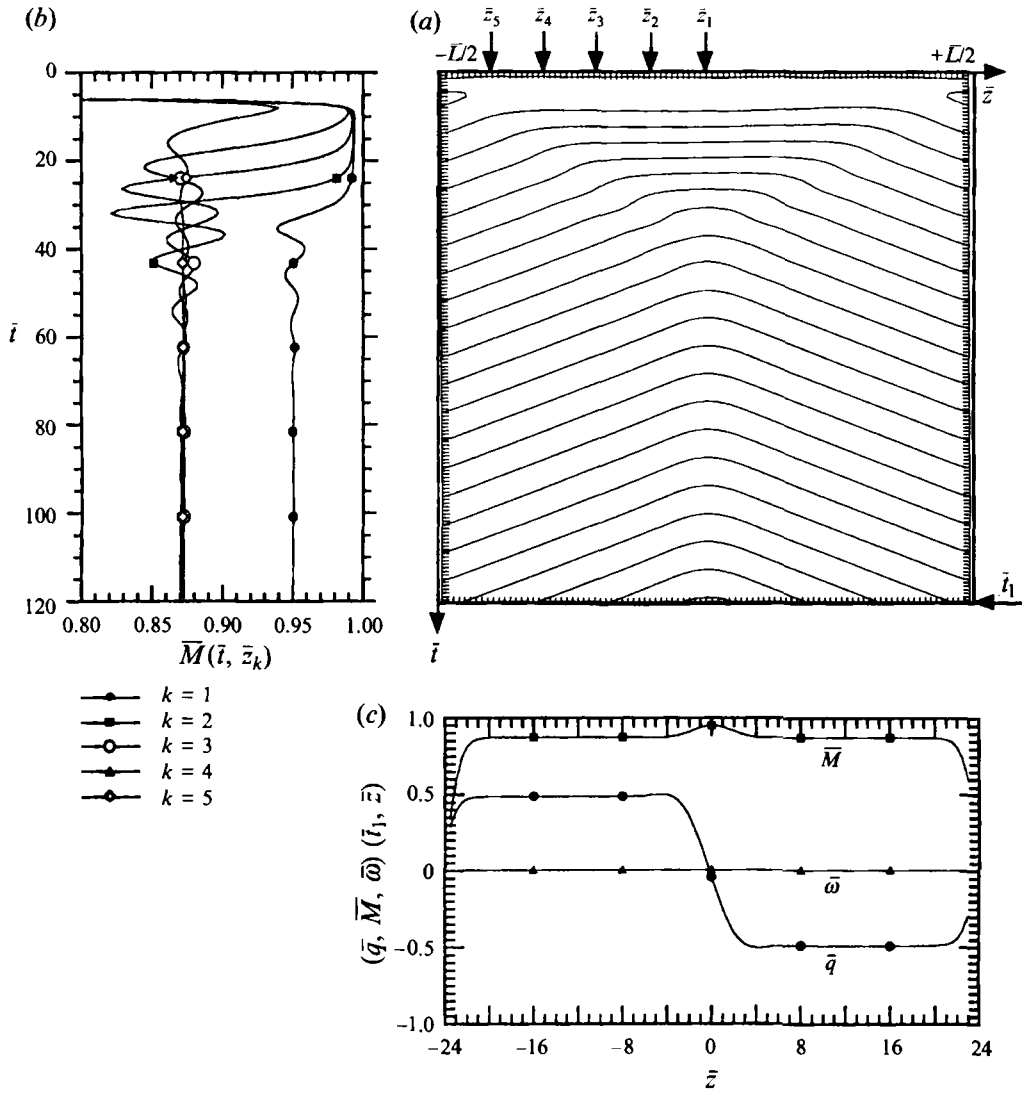

FIGURE 14. The weakly unstable chevron. The following representations are used: (*a*) lines $\mathrm{Re}(\bar{A}(\bar{t},\bar{z})\exp(\mathrm{i}(c_0+\Delta c_0)\bar{t}))\in\{-1,0,1\}$ (pseudo flow visualization), (*b*) functions $\bar{t}\to\bar{M}(\bar{t},\bar{z}_k)$, where $\bar{z}_k=-(\bar{L}/2)(k-1)/5$ and $k\in\{1,2,3,4,5\}$, (*c*) functions $\bar{z}\to(\bar{q},\bar{M},\bar{\omega})(\bar{t},\bar{z})$ at time $\bar{t}_1$. Parameters: $\bar{L}=48$, $c_0=-1.59$ (adapted), $c_1=-0.3$, $c_2=-2$, $\mathrm{d}\bar{t}=0.2$, $\mathrm{d}\bar{z}=0.5$, $\Delta c_0=0.5$.

identical. The experimental instability results from $\bar{q}_\infty((c_1,c_2)(Re))$ crossing the stability boundary in the (c_1,c_2)-plane, at $Re=Re_W$ and for L/d large enough. In experiments (Albarède 1991, figure EXP 19), as well as in the GL model, the instability appears when the spanwise wavenumber (or the shedding angle) becomes too large.

For (c_1,c_2) crossing the stability boundary, we found from numerical simulations that the results were essentially independent of the precise path of (c_1,c_2), at least within the area of physical interest. We give results only for a particular path.

Solutions are illustrated by the following representation:

(*a*) lines, defined by real $(\bar{A}(\bar{t},\bar{z})\exp(\mathrm{i}0.5\bar{t}))=0$, simulate smoke wire flow visualizations (c_0 is adapted, the exponential factor represents vortex advection, as explained in §3.2);

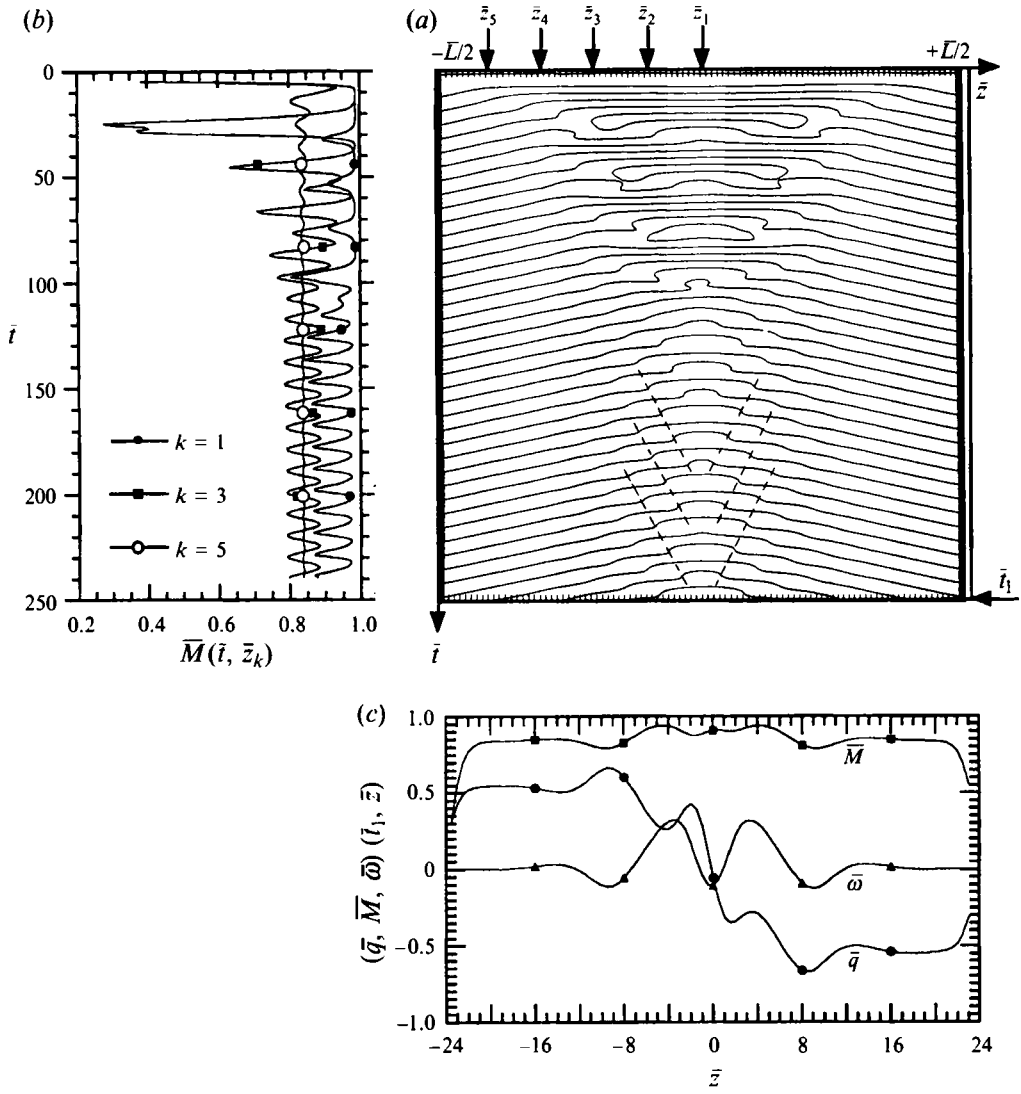

FIGURE 15. The wavy chevron. Same representations as those of figure 14. Dashed line: reverse modulational chevron. Parameters: $\bar{L} = 48$, $c_0 = -1.46$ (adapted), $c_1 = -0.175$, $c_2 = -2$, $d\bar{t} = 0.2$, $d\bar{z} = 0.5$, $\Delta c_0 = 0.5$.

(*b*) plots $\bar{t} \rightarrow \bar{M}(\bar{t}, \bar{z})$ stand for velocity recordings;
(*c*) plots $\bar{z} \rightarrow (\bar{q}, \bar{M}, \bar{\omega})(\bar{t}, \bar{z})$ represent the solution at a given time.

We identified different modes, according to the transient and asymptotic patterns.

(i) 'Robust chevron' (no figure: this classical situation is not illustrated)

In the stable region, well away from the stability boundary, oblique plane waves settle shortly after the Landau transient (of which the rescaled duration is unity).

(ii) 'Weakly unstable chevron' (figure 14)

The vicinity of the stability boundary causes a transient waviness, modulating the oblique plane waves. This waviness is decaying and does not persist in the asymptotic solution.

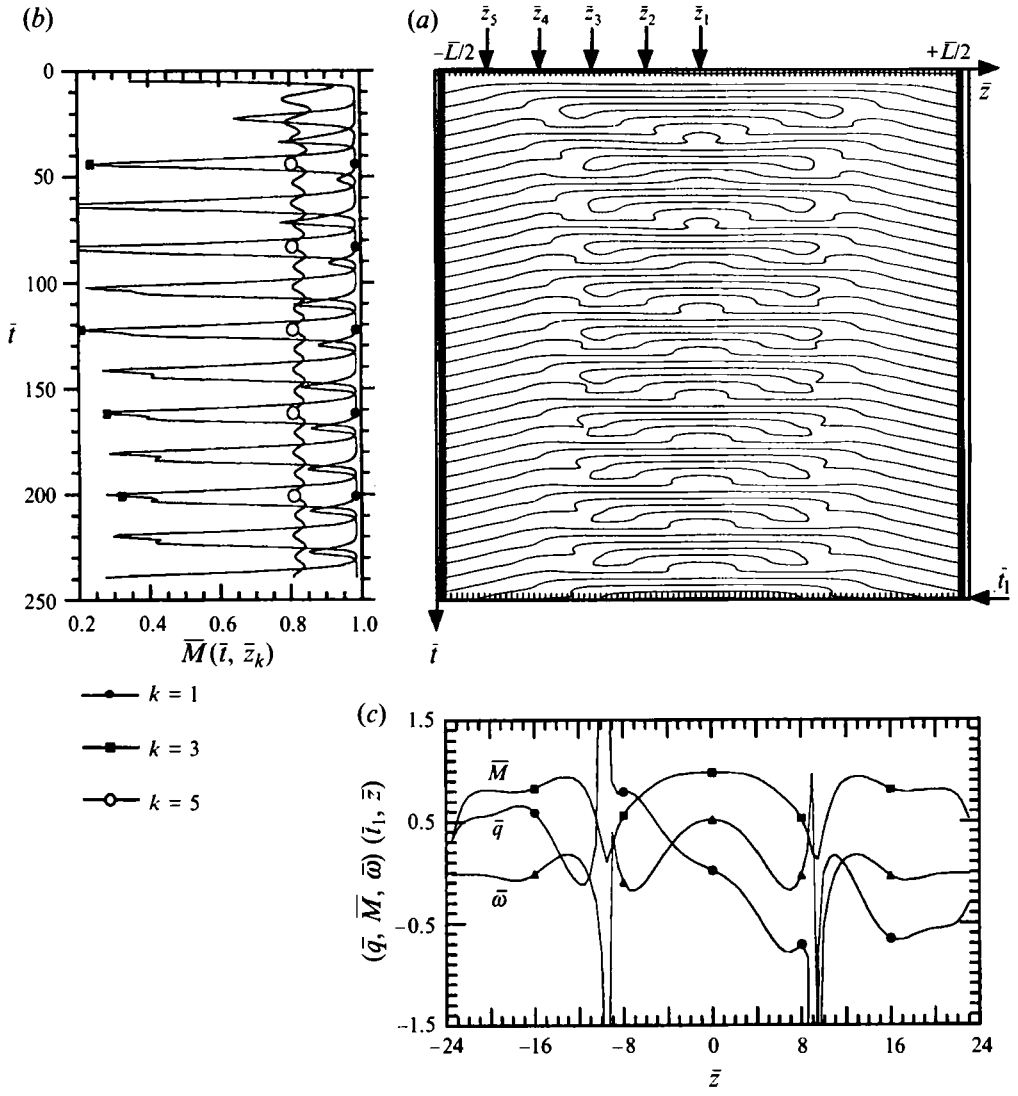

FIGURE 16. The dislocated chevron. Same representations as those of figure 15. Parameters: $\bar{L} = 48$, $c_0 = -1.41$ (adapted), $c_1 = -0.12$, $c_2 = -2$, $\mathrm{d}\bar{t} = 0.2$, $\mathrm{d}\bar{z} = 0.5$, $\Delta c_0 = 0.5$.

(iii) 'Wavy chevron' (figure 15)

Once in the unstable region, the waviness persists in the asymptotic state. The amplitude of waviness is larger near the central phase shock. Isophase lines of waviness also form a chevron, but pointing in a direction opposite to that of the basic chevron (see figure 15*a*)! During the transient, the phase shocks propagating from the ends towards the centre are actually replaced by nodes. These nodes eventually collide with, and annihilate, each other. The asymptotic solution is time-quasi-periodic.

(iv) 'Dislocated chevron' (figure 16)

The nodes already observed in the wavy chevron solution transient persist in the asymptotic state. They create one central cell and two lateral cells. The central cell has a greater frequency and a lower wavenumber than the lateral cells. The central cell frequency is slightly lower than the parallel shedding frequency.

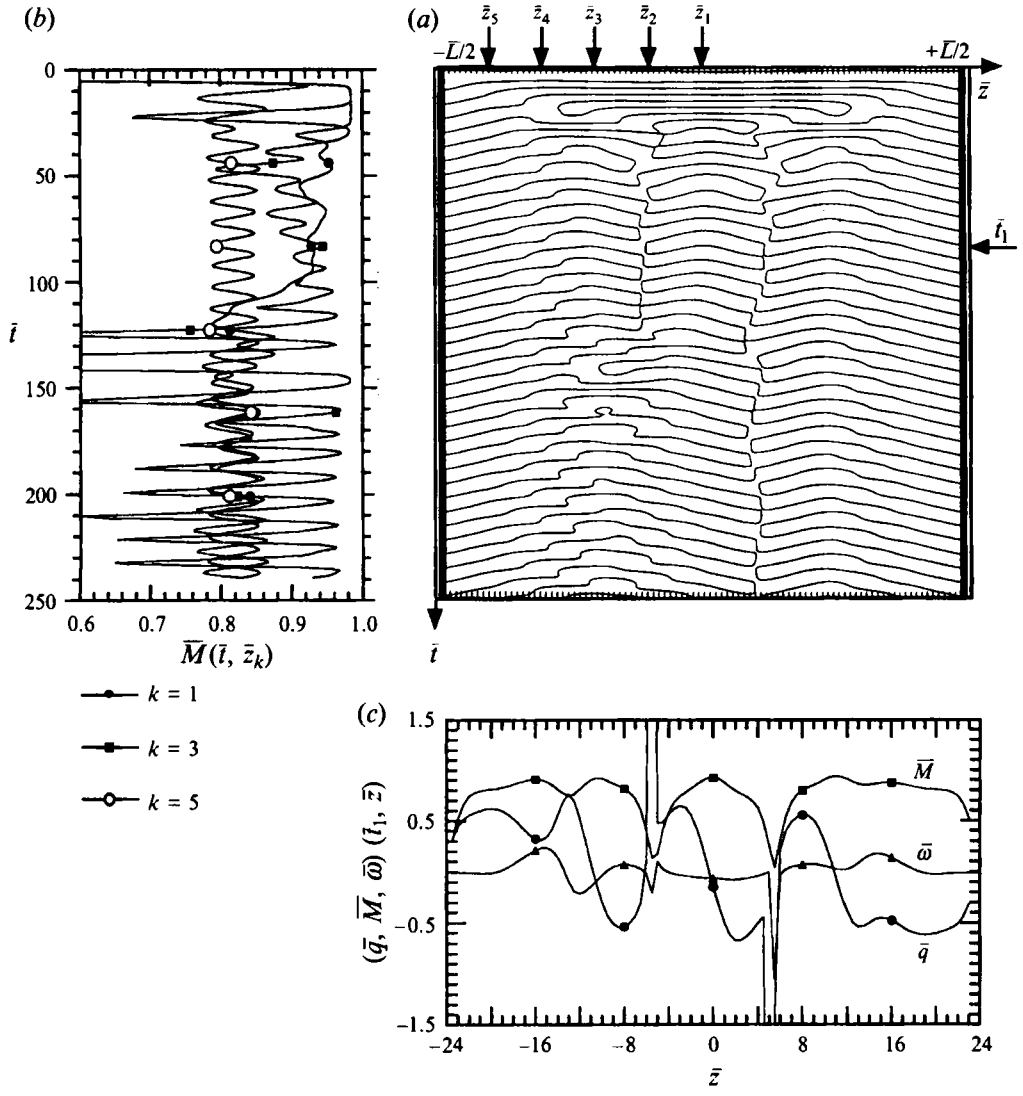

FIGURE 17. The split wake. Same representations as those of figure 15, except that $\bar{t}_1 = 80$ is not the final time. Parameters: $\bar{L} = 48$, $c_0 = -1.38$ (adapted), $c_1 = -0.1$, $c_2 = -2$, $\mathrm{d}\bar{t} = 0.2$, $\mathrm{d}\bar{z} = 0.5$, $\Delta c_0 = 0.5$.

(v) 'Split wake' (figure 17)

The wake is split into three or two cells. Any two neighbouring cells are separated by a node, having identical frequencies, and are in phase opposition (repulsive lock-in). We now have some 'defect dynamics': nodes may move, collide, oscillate, show erratic motion, etc.

We limited our exploration of the GL equation to the phase-diffusion stable case ($1 + c_1 c_2 > 0$). We have time-quasi-periodic or weakly chaotic phenomena. The phase-diffusion unstable case ($1 + c_1 c_2 < 0$), treated by Shraiman *et al.* (1992), is strongly chaotic, and we do not know if it can be applied to the cylinder wake.

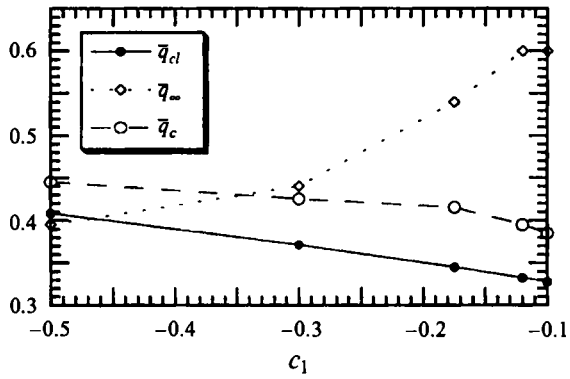

FIGURE 18. Variation of three important spanwise wavenumbers, along the line $c_2 = -2$, for (c_1, c_2) crossing the stability boundary. $\bar{q}_{\infty}(c_1, c_2)$: wavenumber selected by the zero boundary conditions. $\bar{q}_{cl}(c_1, c_2)$: if $\bar{q} > \bar{q}_{cl}$, the plane wave $A_{\bar{q}}$ is linearly unstable with respect to large-wavelength perturbations. $\bar{q}_c(c_1, c_2)$: if $\bar{q} > \bar{q}_c$, the plane wave is unstable in the numerical simulation of the GL equation with periodic boundary conditions and $\bar{L} = 4\pi/\bar{q}$. Numerical parameters: c_0 adapted, $\mathrm{d}\bar{t} = 0.2$, $\mathrm{d}\bar{z} = \bar{L}/96$.

6.3. *Elements of a stability theory*

The linear analysis of the (infinite) plane wave stability was performed by Kuramoto (1984). We recall some of his results: (i) if $1 + c_1 c_2 < 0$, then all plane waves are unstable; (ii) in the opposite case, plane waves with

$$|\bar{q}| > \bar{q}_{cl}(c_1, c_2) = [1 + 2(1 + c_2^2)/(1 + c_1 c_2)]^{-1/2} \tag{6.5}$$

are linearly unstable with respect to large-wavelength perturbations. All plane waves are obviously marginally unstable with respect to a uniform phase shift, that is an infinite-wavelength perturbation.

For each mode, we calculate $\bar{q}_{cl}(c_1, c_2)$ given by (6.5) and the selected wavenumber $\bar{q}_{\infty}(c_1, c_2)$. Quite obviously, the selected oblique plane wave becomes linearly unstable as (c_1, c_2) moves towards the unstable region.

But $\bar{q}_{cl}$ is not fully relevant, because it concerns the linear stability of an infinite plane wave subjected to arbitrarily large-wavelength perturbations, whereas we are interested in the nonlinear stability of a finite plane wave. The consequence of a finite length is that perturbations with a wavelength roughly greater than $\bar{L}$ cannot develop: this is a stabilizing effect.

We numerically investigated the stability of finite plane waves (with wavenumbers $\bar{q}$), in a periodic medium of size $4\pi/\bar{q}$ (for a typical $\bar{q} \approx 0.5$, $4\pi/\bar{q} \approx 24$). The stability condition is $\bar{q} < \bar{q}_c$, where $\bar{q}_c(c_1, c_2)$ is determined numerically by successive trials. The three quantities $\bar{q}_{\infty}$, $\bar{q}_{cl}$, $\bar{q}_c$ are plotted against c_1 (c_2 is constant) in figure 18. The result confirms that the chevron solution instability is very similar to the instability of each finite wave constituting the chevron. The effect of the finite length is mostly a stabilizing effect.

A more advanced theory for the chevron solution stability can be sketched: the departure from the chevron solution would be governed, by, again, a Ginzburg–Landau equation. The linear growth rate results from Kuramoto's (1984) linear study. The nonlinear coefficient would ensure saturation only in the wavy chevron mode, but not in further stages, where a subcritical bifurcation would have to be considered. The initial condition is the strong and random waviness resulting from the Landau amplification of the small initial noise: this explains why the transient of

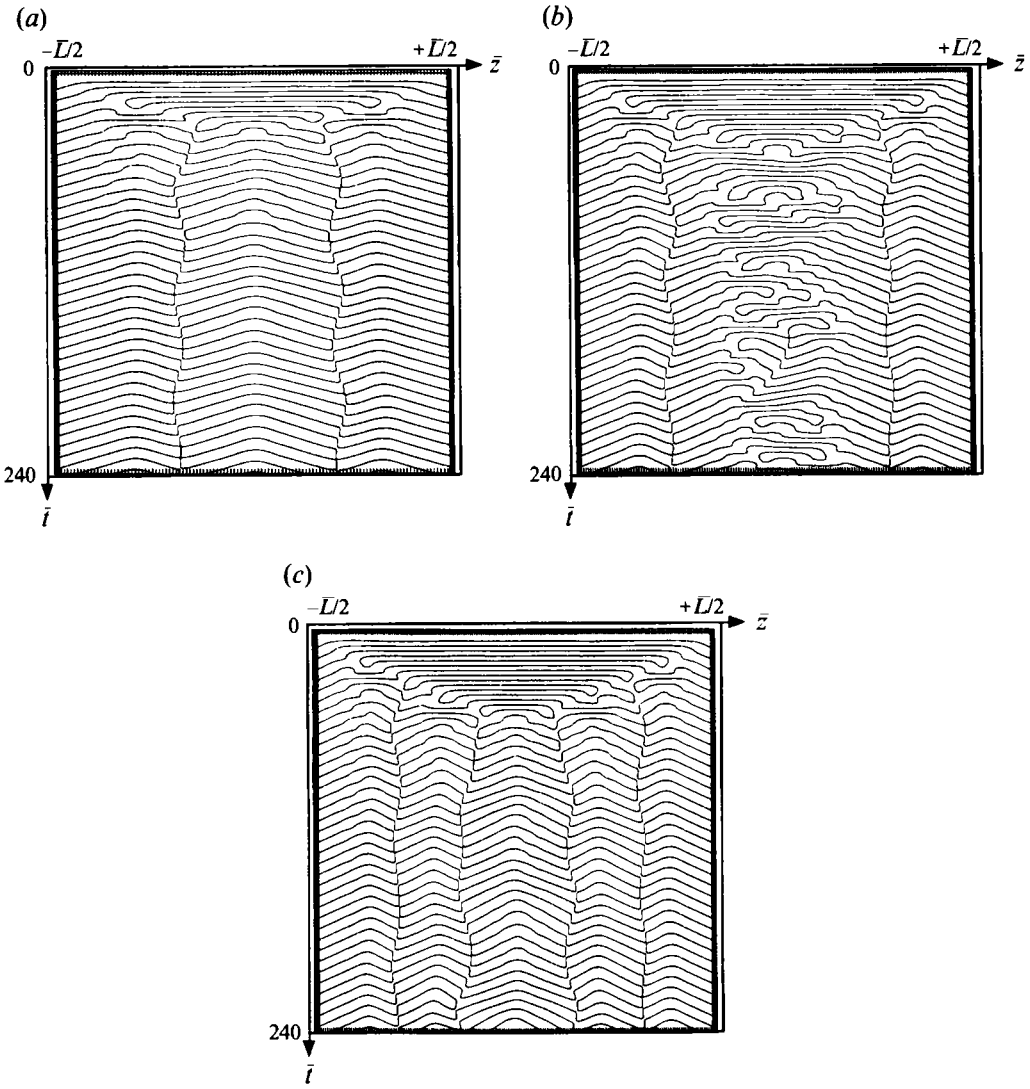

FIGURE 19. The split wake. Lines $\mathrm{Re}(\bar{A}(\bar{t},\bar{z})\exp(\mathrm{i}(c_0+\Delta c_0)\bar{t}))\in\{-1,0,1\}$ (pseudo flow visualization). Parameters: $c_0=-1.41$ (adapted), $c_1=-0.12$, $c_2=-2$, $\mathrm{d}\bar{t}=0.2$, $\mathrm{d}\bar{z}=0.5$, $\Delta c_0=0.5$. (*a*) 3 cells, $\bar{L}=60$; (*b*) 3 or 5 cells, $\bar{L}=84$; (*c*) 5 cells, $\bar{L}=96$.

a given mode contains decaying patterns of the next more unstable mode. Zero boundary conditions, again, would produce the reverse modulational chevron formed by the isophase lines of waviness, in the wavy chevron mode (see figure 15*a*).

6.4. *The finite-length effect in the unstable case*

The stable chevron solution is independent of $\bar{L}$, as soon as the condition (2.28) is realized. In the unstable case, there must be a most unstable mode, with some finite wavelength. The unstable solution will be independent of $\bar{L}$, for $\bar{L}$ much greater than the most unstable wavelength. Accordingly, we investigated the evolution of the dislocated chevron solution when varying $\bar{L}$ (see figure 19).

We define $\bar{L}(N)$ as the length above which the Nth pair of nodes is (symmetrically) created when increasing $\bar{L}$. The onset of the first mode can be considered as the creation

of a pair of bound nodes: hence, $\bar{L}(1) = \pi$ (π is the minimum length of any cell). For $\bar{L} > \bar{L}(1)$, a stable, then wavy, chevron is observed. The wavy chevron breaks and produces a pair of free nodes, for $\bar{L} = \bar{L}(2)$. We notice that the GL model also applies with boundary conditions taken between any two nodes. Therefore, $\bar{L}(2)$ is the maximum size of any cell (a bigger cell would break). By recurrence for all $N \geqslant 2$, $\bar{L}(N)$ exists, and

$$(2N-1)\,\pi \leqslant \bar{L}(N) \leqslant (N-1)\,\bar{L}(2). \tag{6.6}$$

The exact process of node creation is illuminated by numerical simulations, presented for the case $(c_1, c_2) = (-0.12, -2)$, which bears some generality in the vicinity of the stability boundary. Let us start from a symmetrical situation with a central cell and, possibly, lateral cells. The increase of $\bar{L}$ is mainly supported by the central cell. Eventually, it becomes greater than $\bar{L}(2)$ and produces a pair of free nodes, a pair of lateral cells, and a new central cell. The process can be reiterated, and it is an analogue of Russian dolls: the inner cell breaks, leaving two separate lateral cells, and a new cell is created at midspan, and so on.

With the numerical parameters $(c_0, c_1, c_2) = (-1.41, -0.12, 2)$, $\mathrm{d}\bar{t} = 0.2$, $\mathrm{d}\bar{z} = 0.5$, the minimum size of the central cell was about 13; $33 < \bar{L}(2) < 36$, $60 < \bar{L}(3) < 96$, and $N = 6$ at $\bar{L} = 240$. In practice, if $\bar{L} \gtrsim \bar{L}(3)$, the free nodes have oscillatory movements or disappear intermittently, so that the above process is much disturbed. The solution (specifically the existence of nodes) can be sensitive to initial conditions. Lateral cells form dissymetrical chevrons, evolving continuously with increasing $\bar{L}$ from isolated finite plane waves to symmetrical chevrons. More precisely, every finite plane wave is shorter than 10, while the total length of a lateral cell is 10, 12, 16, 19 for $\bar{L} = 33$, 48, 60, 240.

6.5. *A comparison between experiments and the model for the unstable large-$\bar{L}$ case*

We have shown that an increase of $\bar{L}(Re, L/d)$, as well as a variation of $(c_1, c_2)(Re)$, can induce instability and node creation. In experiments, the instability develops when decreasing Re to below Re_W, and Re_W does not depend on L/d (Williamson 1989): hence, the transition can be caused only by the variation of (c_1, c_2) with Re. For a typical $Re < Re_W$, e.g. $Re = 58.5$, the Kuramoto lengthscale given by (4.8) is about $2.2d$. The stable (or wavy) chevron flow should be obtained for $\pi \ll \bar{L} < \bar{L}(2)$ or $7 \ll L/d < 73$; the split wake should be obtained for $\bar{L}(2) \ll \bar{L} < \bar{L}(3)$ or $79 \ll L/d < 132$.

Williamson's (1989) range was $70 < L/d < 240$, and, for $Re < Re_W$, he has identified only the dislocated chevron. He did not report the stable chevron (for L/d small enough), although we know for certain from our small-$\bar{L}$ experiments that this mode exists; neither did he report the split wake: this mode remains to be observed. The wavy chevron can be recognized on Williamson's (1989) figure 7(*b*), with many features of the numerical solution (see above), in particular the reverse modulational chevron.

König *et al.* (1990) observed various transitions in large-L situations, depending on the end configuration. In the case of end plates, the wake has two eigenmodes, corresponding to parallel shedding and oblique shedding. In the case of wind-tunnel wall boundary layers, the wake has the same eigenmodes, plus one that does not obviously appear in our exploration of the GL model.

7. Conclusion

Most of the three-dimensional and time-quasi-periodic phenomena (summarized in figure 20) have been explained at least qualitatively by means of the GL model.

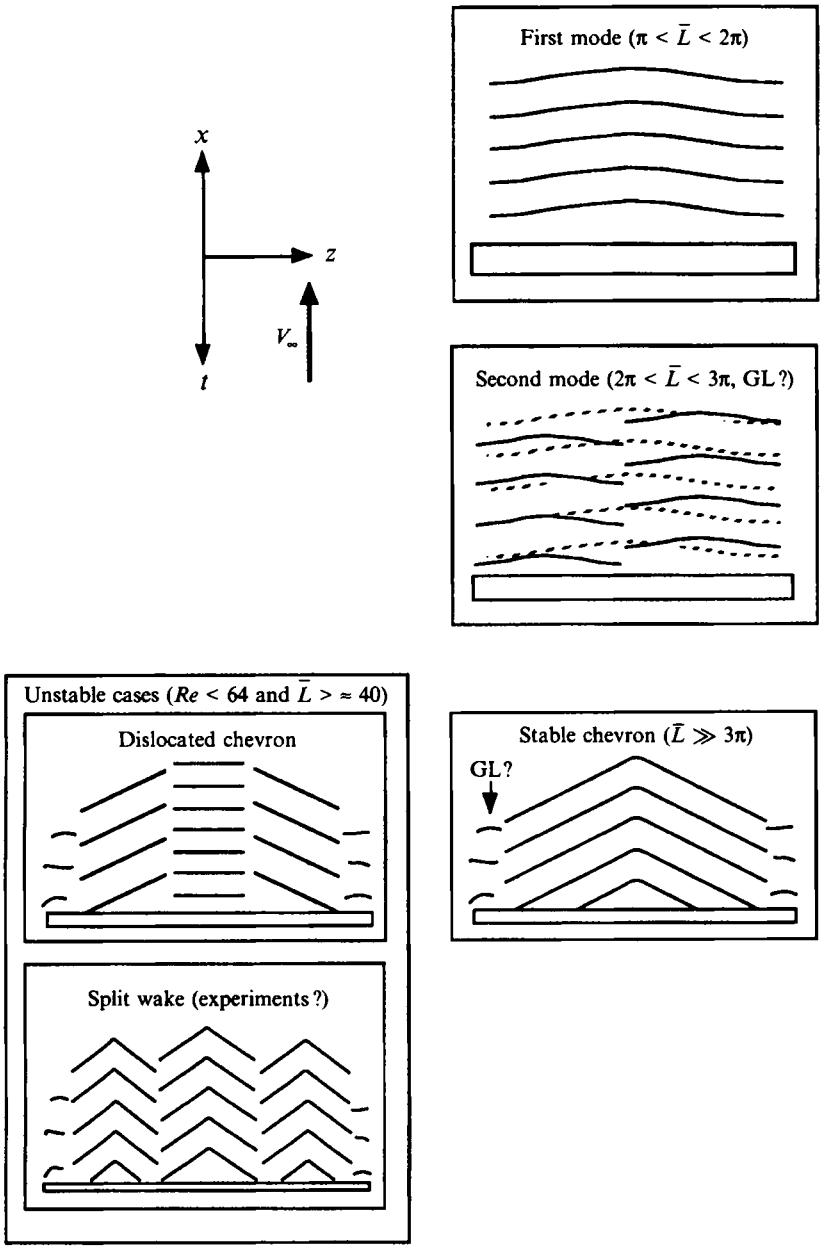

FIGURE 20. Summary of discussed wake patterns and GL model solutions.

Fundamental wake parameters are the Reynolds number Re and the aspect ratio L/d. They participate in the GL model through $\bar{L}(Re, L/d)$ and $(c_1, c_2)(Re)$. The latter dependence is particularly important when it causes a secondary instability, leading to the dislocated chevron. The GL model gives a unified vision of very different facts, and illuminates many old controversies. It is at least a good framework for presenting experimental results pertaining to weakly three-dimensional wakes (or possibly shear flows) with supercritial absolute instabilities. In the course of this study, some mathematical features of the GL equation have been discovered.

At least one wake parameter, say the dimensionless fetch F/d, must be introduced

to represent the end configuration, since different flows can be observed with identical parameters $(Re, L/d)$, but different end conditions. The GL model is not ideally suited to represent the fully three-dimensional end configuration. In particular, the boundary conditions must be applied with care. Also, the second mode seems to be sustained by the end-plate boundary layers, through some unidentified energy transfer process. End effects can be suppressed by considering the wake of a torus, which has no ends (Leweke *et al.* 1993). However, the correct understanding of the end flow, and its interaction with the rest of the flow remains a difficult but important problem.

The model can be improved in many ways, in order to get a better representation of experimental results. For example, the streamwise coordinate can be implemented (Rossi, Huerre & Redekopp 1989, Park & Redekopp 1992). The quality of experimental results will have to be improved if further developments are to be undertaken. In particular, the accuracy of the rescaled model coefficients should be reduced to ± 0.1, and the variations with the Reynolds number should be determined.

We thank F. Abetino and J. Minelli for their technical assistance and L. Boyer, T. Leweke, P. Monkewitz for fruitful discussions. This work has benefited from the financial support of the EEC under contract No. SC1-0212-C(TT) and Action Incitative en Mecanique des Fluides DPST8 Ministère de l'Enseignement Supérieur et de la Recherche.

Appendix. The link between the complex amplitude A and the observable fields

We propose the following expansion for any component of the velocity field:

$$v(t,x,y,z,Re) = V_{00}(x,y,Re) + A(t,z,Re)\,V_{10}(x,y,Re) + A^* V_{01} + A^2 V_{20} + AA^* V_{11} + A^{*2} V_{02} + \ldots$$

or, more explicitly:

$$v(t,x,y,z,Re) = \sum_{n_1,n_2\geqslant 0} A(t,z,Re)^{n_1} A^*(t,z,Re)^{n_2} V_{n_1,n_2}(x,y,Re). \tag{A 1}$$

The reality of v implies

$$V_{n_1,n_2} = V^*_{n_2,n_1}. \tag{A 2}$$

The V_{n_1,n_2} are the basic flow (for $n_1 = n_2 = 0$), the linear modes ($n_1+n_2 = 1$), and nonlinear modes ($n_1+n_2 > 1$), of the plane wake. Nonlinear modes are generated by the quadratic nonlinearity of the momentum Navier–Stokes equation.

This representation has the following qualities.

(i) If $|A|$ does not depend on time, then the time-average of the velocity component is

$$\langle v\rangle = \sum_{n\geqslant 0} |A|^{2n} V_{n,n}. \tag{A 3}$$

For a finite amplitude, the average flow differs from the basic flow, which is a typical nonlinear effect.

(ii) Harmonics are included. In particular, if A is a linear combination of $\exp(\mathrm{i}\omega_1 t)$ and $\exp(\mathrm{i}\omega_2 t)$, then the linear combinations of ω_1 and ω_2 are also produced, in agreement with observations of nonlinear mixing reported in Albarède (1989).

(iii) In a time-periodic regime, the vortex street is alternating, and this can be accounted for by the fundamental streamwise velocity component vanishing at $y = 0$:

$$V_{10x}(x, 0, Re) = 0. \tag{A 4}$$

(The subscript x means the x-component.)

Since the velocity measurements are most often performed on a segment $\{(x_0, y_0, z), -L/2 < z < +L/2\}$ and for some component V_i, $i \in \{x, y, z\}$, it is convenient (and possible) to impose

$$V_{10i}(x_0, y_0, Re) = 1/2. \tag{A 5}$$

For $i = x$, because of (A 4), y_0 must not be zero (otherwise, the normalization is impossible). Omitting the harmonics in (A 1) and using (A 5), we obtain a simplified expression,

$$v_i(t, x_0, y_0, z, Re) = V_{00i}(x_0, y_0, Re) + \mathrm{Re}[A(t, z, Re)]. \tag{A 6}$$

The amplitude of the velocity fluctuation as a function of all space coordinates and Re involves the variations of $V_{10}(x, y, Re)$, according to (A 1). Some results of Mathis (1983) are indeed measurements of the dependence $(x, Re) \to V_{10y}(x, 0, Re)$. This problem was also recently treated by Jenffer *et al.* (1992).

REFERENCES

ALBARÈDE, P. 1989 Perturbations tridimensionnelles du sillage d'un cylindre à bas nombre de Reynolds. Stage de Magistère Interuniversitaire de Physique, Université Paris 6.

ALBARÈDE, P. 1991 Auto-organisation dans le sillage 3D d'un obstacle non profilé. Thèse Université de Provence. (English version available from LRC: Self-organization in the 3D wakes of bluff bodies.)

ALBARÈDE, P., LEWEKE, T. & PROVANSAL, M. 1992 The Ginzburg–Landau equation as a model of the three-dimensional circular cylinder at low Reynolds numbers. *IUTAM Symp. on Bluff Body Wakes, Dynamics and Instabilities, September 1992, Göttingen, Germany*, pp. 7–11.

ALBARÈDE, P. & MONKEWITZ, P. A. 1992 A model for the formation of oblique shedding and 'chevron' patterns in cylinder wakes. *Phys. Fluids* A **4**, 744–756.

ALBARÈDE, P., PROVANSAL, M. & BOYER, L. 1990 Modélisation par l'équation de Ginzburg–Landau du sillage tridimensionnel d'un obstacle allongé. *C. R. Acad. Sci. Paris* **310** (II), 459–464.

BERGER, E. 1967 Suppression of vortex shedding and turbulence behind oscillating cylinders. *Phys. Fluids* suppl. S191–S193.

BERGER, E. & WILLE, R. 1972 Periodic flow phenomena. *Ann. Rev. Fluid Mech.* **4**, 313–340.

CHIFFAUDEL, A. 1992 Non-linear stability analysis of two-dimensional patterns in the wake of a circular cylinder. *Europhys. Lett.* **18**, 589–594.

DAVEY, A., HOCKING, L. M. & STEWARTSON, K. 1974 On the nonlinear evolution of three-dimensional disturbances in plane Poiseuille flow. *J. Fluid Mech.* **63**, 529–536.

DUSĚK, J., LE GAL, P. & FRAUNIÉ, P. 1994 A numerical and theoretical study of the first Hopf bifurcation in a cylinder wake. *J. Fluid Mech.* **264**, 59–80.

GASTER, M. 1969 Vortex shedding from slender cones at low Reynolds number. *J. Fluid Mech.* **38**, 565–576.

GASTER, M. 1971 Vortex shedding from circular cylinders at low Reynolds number. *J. Fluid Mech.* **46**, 749–756.

GERICH, D. 1987 A limiting process for the von Kármán vortex street showing the change from two- to three-dimensional flow. *Proc. 4th Intl Symp. on Flow Visualization.*

GERICH, D. & ECKELMANN, H. 1982 Influence of end plates and free ends on the shedding frequency of circular cylinders. *J. Fluid Mech.* **122**, 109–121.

GERRARD, J. H. 1966 The three-dimensional structure of the wake of a circular cylinder. *J. Fluid Mech.* **25**, 143–164.

GERRARD, J. H. 1978 The wakes of cylindrical bluff bodies at low Reynolds number. *Phil. Trans. R. Soc. Lond.* A **288**, 351.

HAMA, F. R. 1957 Three-dimensional vortex pattern behind a circular cylinder. *J. Aeronaut. Sci.* **24**, 156.

HUERRE, P. & MONKEWITZ, P. A. 1990 Local and global instabilities in spatially developing flows. *Ann. Rev. Fluid Mech.* **22**, 473–537.

JENFFER, P., WESFREID, J. E., GOUJON-DURAND, S., BÉNARD, R. & BOUSSORA, R. 1992 Spatial properties along the flow of the vortex emission behind a bluff body. *Proc. IUTAM Symp. on Bluff-Body Wakes, Dynamics, and Instabilities, Göttingen, Sept. 7–11.*

KÖNIG, M., EISENLOHR, H. & ECKELMANN, H. 1990 The fine structure in the Strouhal–Reynolds number relationship of the laminar wake of a circular cylinder. *Phys. Fluids* A **2**, 1607–1614.

KURAMOTO, Y. 1984 *Chemical Oscillations, Waves, and Turbulence*. Springer.

LANDAU, L. & LIFCHITZ, E. 1971 *Mécanique des fluides*. Moscow: Mir.

LE DIZES, S., MONKEWITZ, P. A. & HUERRE, P. 1992 Weakly nonlinear analysis of spatially developing shear flows. *Proc. IUTAM Symp. on Bluff-Body Wakes, Dynamics, and Instabilities, Göttingen, Sept. 7–11.*

LEE, T. & BUDWIG, R. 1991 A study of the effect of aspect ratio on vortex shedding behind circular cylinders. *Phys. Fluids* A **3**, 309–315.

LEWEKE, T. & PROVANSAL, M. 1994 Determination of the parameters of the Ginzburg–Landau wake model from experiments on a bluff ring. *Europhys. Lett.* **27**, 655–660.

LEWEKE, T., PROVANSAL, M. & BOYER, L. 1993 Sillage tridimensionnel d'un obstacle torique et modélisation par l'equation de Ginzburg–Landau. *C.R. Acad. Sci. Paris* **316** (II), 287–292.

MATHIS, C. 1983 Propriétés des composantes de vitesse transverses dans l'écoulement de Bénard – von Kármán aux faibles nombres de Reynolds. Thèse, Université de Provence.

MATHIS, C., PROVANSAL, M. & BOYER, L. 1984*a* The Bénard–von Kármán instability: an experimental study near the threshold. *J. Phys. Lett. Paris* **45**, L-483–L-491.

MATHIS, C., PROVANSAL, M. & BOYER, L. 1984*b* The rotating grating applied to the study of the Bénard–von Kármán instability near the threshold. *Proc. Second Intl Symp. on Applications of Laser Anemometry to Fluid Mechanics, Lisbon.*

MONKEWITZ, P. A. 1988 The absolute and convective nature of instability in two-dimensional wakes at low Reynolds number. *Phys. Fluids* **31**, 999–1006.

NOACK, B. & ECKELMANN, H. 1991 Two-dimensional, viscous, incompressible flow around a circular cylinder. *Max Planck Institut für Strömungsforschung, Göttingen, Bericht* 104/1991.

NOACK, B., OHLE, F. & ECKELMANN, H. 1991 On cell formation in vortex streets. *J. Fluid Mech.* **227**, 293–308.

NOZAKI, B. & BEKKI, N. 1984 Exact solutions of the generalized Ginburg–Landau equation. *J. Phys. Soc. Japan* **53**, 1581–1582.

PAPANGELOU, A. 1992 Vortex shedding from slender cones at low Reynolds numbers. *J. Fluid Mech.* **242**, 299–321.

PARK, D. S. & REDEKOPP, L. G. 1992 Selection principles for spatio-temporal patterns in wake flows. *Proc. IUTAM Symp. on Bluff-Body Wakes, Dynamics, and Instabilities, Göttingen, Sept. 7–11.*

PROVANSAL, M. 1988 Etude expérimentale de l'instabilité de Bénard–von Kármán. Thèse, Universitè de Provence.

PROVANSAL, M., LEWEKE, T. & ALBARÈDE, P. 1992 Visualisation du sillage d'un obstacle au moyen de nappes de fumée: mise en évidence des effets tridimensionnels. *5ème Colloque National de Visualisation et de Traitement d'Images en Mécanique des Fluides, 2–5 Juin 1992, Poitiers.*

PROVANSAL, M., MATHIS, C. & BOYER, L. 1987 Bénard–von Kármán instability: transient and forced regimes. *J. Fluid Mech.* **182**, 1–22.

ROSSI, M., HUERRE, P. & REDEKOPP, L. G. 1989 A model of boundary effects in Kármán vortex streets. *Bull. Am. Phys. Soc.* **34**, 2282.

SCHUMM, M., BERGER, E. & MONKEWITZ, P. A. 1994 Self-excited oscillations in the wake of two-dimensional bluff bodies and their control. *J. Fluid Mech.* **271**, 17–53.

SHRAIMAN, B. I., PUMIR, A., SAARLOOS, W. VAN, HOHENBERG, P. C. & CHATÉ, H. 1992 Spatiotemporal chaos in the one-dimensional complex Ginzburg–Landau equation. *Physica* D **57**, 241–248.

SLAOUTI, A. & GERRARD, J. H. 1981 An experimental investigation of the end effects on the wake

of a circular cylinder towed through water at low Reynolds numbers. *J. Fluid Mech.* **112**, 297–314.

SREENIVASAN, K. R. 1985 Transition and turbulence in fluid flows and low-dimensional chaos. In *Frontiers in Fluid Mechanics* (ed. S. H. Davis & J. L. Lumley), pp. 41–67. Springer.

STRYKOWSKI, P. J. 1986 The control of absolutely and convectively unstable flows. PhD thesis, Yale University.

TRITTON, D. J. 1959 Experiments on the flow past a circular cylinder at low Reynolds numbers. *J. Fluid Mech.* **6**, 547–567.

TRITTON, D. J. 1971 A note on vortex streets behind circular cylinders at low Reynolds numbers. *J. Fluid Mech.* **45**, 203–208.

VAN ATTA, C. W. & GHARIB, M. 1987 Ordered and chaotic vortex streets behind circular cylinders at low Reynolds numbers. *J. Fluid Mech.* **174**, 113–133.

WILLIAMSON, C. H. K. 1988 The existence of two stages in the transition to three-dimensionality of a cylinder wake. *Phys. Fluids* **31**, 3165–3168.

WILLIAMSON, C. H. K. 1989 Oblique and parallel modes of vortex shedding in the wake of a circular cylinder at low Reynolds numbers. *J. Fluid Mech.* **206**, 579–627.